

Lower soil moisture and deep soil temperatures in thermokarst features increase old soil carbon loss after 10 years of experimental permafrost warming

Elaine F. Pegeraro^{1,2}  | Marguerite E. Mauritz³  | Kiona Ogle^{1,4} 
 Christopher H. Ebert¹  | Edward A. G. Schuur^{1,2} 

¹Center for Ecosystem Science and Society, Northern Arizona University, Flagstaff, AZ, USA

²Biological Sciences, Northern Arizona University, Flagstaff, AZ, USA

³Ecology and Evolutionary Biology, The University of Texas at El Paso, El Paso, TX, USA

⁴School of Informatics, Computing, and Cyber Systems, Northern Arizona University, Flagstaff, AZ, USA

Correspondence and present address
 Elaine F. Pegeraro, Climate Sciences Department, Climate and Ecosystem Sciences Division, Lawrence Berkeley National Laboratory, Berkeley, CA 94720, USA.

Email: ElainePegeraro@lbl.gov

Funding information

National Parks Inventory and Monitoring Program; U.S. Department of Energy, Grant/Award Number: DE-SC0006982 and DE-SC0014085; National Science Foundation, Grant/Award Number: 1026415 and 0747195; The Scientific Research Society

Abstract

Almost half of the global terrestrial soil carbon (C) is stored in the northern circumpolar permafrost region, where air temperatures are increasing two times faster than the global average. As climate warms, permafrost thaws and soil organic matter becomes vulnerable to greater microbial decomposition. Long-term soil warming of ice-rich permafrost can result in thermokarst formation that creates variability in environmental conditions. Consequently, plant and microbial proportional contributions to ecosystem respiration may change in response to long-term soil warming. Natural abundance $\delta^{13}\text{C}$ and $\Delta^{14}\text{C}$ of aboveground and belowground plant material, and of young and old soil respiration were used to inform a mixing model to partition the contribution of each source to ecosystem respiration fluxes. We employed a hierarchical Bayesian approach that incorporated gross primary productivity and environmental drivers to constrain source contributions. We found that long-term experimental permafrost warming introduced a soil hydrology component that interacted with temperature to affect old soil C respiration. Old soil C loss was suppressed in plots with warmer deep soil temperatures because they tended to be wetter. When soil volumetric water content significantly decreased in 2018 relative to 2016 and 2017, the dominant respiration sources shifted from plant aboveground and young soil respiration to old soil respiration. The proportion of ecosystem respiration from old soil C accounted for up to 39% of ecosystem respiration and represented a 30-fold increase compared to the wet-year average. Our findings show that thermokarst formation may act to moderate microbial decomposition of old soil C when soil is highly saturated. However, when soil moisture decreases, a higher proportion of old soil C is vulnerable to decomposition and can become a large flux to the atmosphere. As permafrost systems continue to change with climate, we must understand the thresholds that may propel these systems from a C sink to a source.

KEY WORDS

climate change feedback, dual-carbon isotope mixing model, ecosystem respiration, permafrost, radiocarbon, thermokarst

1 | INTRODUCTION

Permafrost is perennially frozen ground that has accumulated 1460–1600 Pg (1 Pg = 1 billion tons) of soil organic carbon (C) globally since the late Pleistocene and Holocene due to freezing temperatures (Hugelius et al., 2014; Pries et al., 2012; Schuur et al., 2015, 2018; Tarnocai et al., 2009; Zimov et al., 2006). Since the 1850–1900 period, human activity has increased air and sea surface temperatures by 0.8–1.2°C, at a rate of 0.2°C per decade (Allen et al., 2019). In high latitudes, air temperatures are increasing about two times faster than the global average (Overland et al., 2019). As the Earth warms, permafrost thaws (Romanovsky et al., 2012) and the northern circumpolar permafrost region becomes increasingly vulnerable to greater microbial decomposition and C loss to the atmosphere (Schuur et al., 2008, 2015).

The potential for Arctic and sub-Arctic ecosystems to store C on an annual basis depends on the equilibrium between gross primary production and the C released from plant and microbial respiration (i.e., ecosystem respiration; R_{eco} ; Chapin et al., 2006). Increased R_{eco} that is driven by plant respiration is likely to be offset by C uptake in aboveground (AG) and belowground (BG) plant biomass and enhanced plant productivity under warmer conditions (Shaver et al., 1986). However, increased R_{eco} that is driven by greater microbial respiration, especially from the decomposition of old soil C that cycles on centennial to millennial time scales, can amplify the permafrost feedback to climate change (Abbott et al., 2016; Davidson & Janssens, 2006; Hobbie & Chapin, 1998; Pries et al., 2013, 2016; Schuur et al., 2009). Plant and microbial respiration respond differently to biological and environmental drivers (Bond-Lamberty et al., 2004); thus, the relative influence of these R_{eco} components could shift in response to changes in soil moisture and temperature that occur with climate change.

Experiments that investigate warming effects on permafrost processes have found that R_{eco} increases with higher soil temperatures (Dorrepaal et al., 2009; Hobbie & Chapin, 1998; Lupascu, Welker, Seibt, Maseyk, et al., 2014; Mauritz et al., 2017; Natali et al., 2011; Oberbauer et al., 2007). Studies from a long-term soil warming experiment, the Carbon in Permafrost Experimental Heating Research (CiPEHR), demonstrated that R_{eco} and gross primary productivity (GPP) initially increased linearly with warmer soil temperatures and deeper permafrost thaw due to enhanced plant productivity (Natali et al., 2012; Salmon et al., 2016). But after 7 years, R_{eco} increased at a faster rate than GPP as plant productivity leveled off (Mauritz et al., 2017). These changes suggest a stronger contribution of microbial respiration to R_{eco} over time (Mauritz et al., 2017), yet these integrated ecosystem-scale flux measurements do not provide mechanistic information on the sources driving permafrost C loss.

Carbon isotopes and associated isotope mixing models can be used to elucidate relative contributions of plant and microbial respiration to R_{eco} (Schuur & Trumbore, 2006; Trumbore, 2000). The stable C isotope (^{13}C) can be applied to separate C sources based on their isotopic composition due to biological fractionation (Bowling

et al., 2008; Fry, 2007). Plant respiration has a similar $^{13}\text{C}/^{12}\text{C}$ ratio as plant tissue (Lin & Ehleringer, 1997) with root respiration being more depleted in ^{13}C relative to AG respiration due to the metabolism of lipid compounds (Bowling et al., 2008). Microbial metabolism, on the other hand, strongly favors the lighter isotope, ^{12}C (Trumbore, 2006). Soil organic matter becomes more decomposed and processed with depth, and the ^{13}C composition ($\delta^{13}\text{C}$) of bulk soil C can increase up to 6‰ from the surface down to ~85 cm (Mauritz et al., 2019; Pries et al., 2013; Schuur et al., 2003). Stable C isotope data can be complemented by radiocarbon (^{14}C) to provide further insight on R_{eco} source contributions. For example, ^{14}C composition of respiration carbon dioxide (CO_2) can be used to estimate the age of C since it was fixed via photosynthesis and its transit time in each C reservoir (Trumbore, 2000). Carbon that is actively cycling on annual to decadal timescales will reflect the bomb enrichment of atmospheric ^{14}C , and C that is cycling on the order of hundreds to thousands of years will have undergone radiocarbon decay and will be depleted in ^{14}C (Trumbore et al., 2016). Implementing both C isotopes supplies a mixing model with more information, thus allowing for better resolution of multiple source contributions to R_{eco} (Schuur et al., 2016).

At CiPEHR, 10 years of experimental soil warming using snow fences and open-top chambers led to a two-fold increase in thaw depth (TD) relative to control plots (Mauritz et al., 2017). The degradation of ice-rich permafrost has resulted in thermokarst formation across the landscape, caused by soil subsidence from the loss of ice structures (Plaza et al., 2019; Rodenhizer et al., 2020). As the surface of the soil moves closer to the water table, soil becomes waterlogged (Lawrence et al., 2015; Nauta et al., 2015). These thermokarst features affect plant and microbial responses by creating spatial and temporal variability in soil moisture (Schuur & Mack, 2018), and inundated conditions can shift vegetation composition, as well as cause shrub and grass mortality (Li et al., 2017). At our site, the initial increase in R_{eco} in the first 4 years of warming (2009–2012) was driven by higher plant respiration, which increased by 30% with warming (Pries et al., 2016). Nevertheless, plant biomass has declined since 2013, especially in inundated plots (Taylor et al., 2018).

This interaction between soil moisture and plant productivity after 10 years of permafrost thaw prompted us to ask the question: did the proportion of R_{eco} from old soil C increase with changing environmental conditions (e.g., soil moisture and temperature) associated with thermokarst formation across the landscape? We hypothesized that the proportion of old soil C loss would increase (1) with permafrost thaw and warmer soil temperatures due to enhanced microbial decomposition at depth where the bulk of the soil C pool has accumulated over many millennia (Pries et al., 2012), and (2) in plots experiencing fluctuation in soil moisture due to greater oxygen (O_2) availability for microbial decomposition at depth. Natural abundance $\delta^{13}\text{C}$ and $\Delta^{14}\text{C}$ of plant AG and BG, surface young soil (0–25 cm; YS), and deep old soil (>25 cm; OS) were used to inform a dual-C isotope mixing model to directly partition the contribution of each source to the total R_{eco} fluxes from 2016 to 2018. We employed a hierarchical Bayesian model approach to partitioning that incorporated GPP and environmental drivers to help constrain the contribution of each

source to improve predictions of the future state of permafrost and its climate forcing potential.

2 | METHODS

2.1 | Field study

The site is located in Eight Mile Lake, Alaska ($63^{\circ}52'59''\text{N}$, $149^{\circ}13'32''\text{W}$) in the ancestral land of the Tanana Athabaskan people, where the mean annual average temperature is -1.0°C , and the mean annual precipitation is 378 mm (Schuur et al., 2009). The organic horizon is ~35 cm thick with C concentrations exceeding 20% (Natali et al., 2011; Plaza et al., 2019; Pries et al., 2012). The cryoturbated mineral soil is classified as Gelisol and comprises glacial till, windblown loess, quartz, and feldspars, and is underlain entirely by permafrost (Osterkamp et al., 2009). A 30 m borehole that was installed in 1985 at Eight Mile Lake (located ~1–1.5 km from our study site) shows that ground temperature data ~15 m is close to 0°C , indicating that permafrost in this region is vulnerable to thaw (Osterkamp & Romanovsky, 1999).

The site is moist acidic tundra, dominated by *Eriophorum vaginatum*, and includes *Carex bigelowii*, *Vaccinium uliginosum*, *Betula nana*, *Rubus chamaemorus*, *Empetrum nigrum*, *Rhododendron subarcticum*, *Vaccinium vitis-idaea*, *Andromeda polifolia*, and *Oxycoccus microcarpus*. Nonvascular plants comprise *Pleurozium schreberi* and *Sphagnum* species, as well as several lichen species (primarily *Cladonia* spp.; Deane-Coe et al., 2015; Natali et al., 2011; Schuur et al., 2007).

2.1.1 | Experimental framework

This study leveraged the long-term Carbon in Permafrost Experimental Heating and Drying Research (CiPEHR and DryPEHR) experiments (Natali et al., 2011, 2015). The soil warming experiment (CiPEHR) began in October of 2008, where soil and permafrost warming was achieved with snow fences ($1.5 \text{ m} \times 8 \text{ m}$) during the winter. Fences were installed perpendicular to dominant winter winds so that snow was deposited on the leeward side of each fence. In the spring, excess snow was removed to ambient levels to achieve similar timing of snowmelt relative to the control side of the fence. In the growing season, polycarbonate open top chambers were used to simulate air warming. The water table manipulation experiment (DryPEHR) began in 2011 within the footprint of CiPEHR. Metal sheets were installed 0.6 m into the ground ($2.5 \text{ m} \times 1.5 \text{ m}$), and pumps were used to lower the water table. Treatments were applied in a split-plot design for a total of 11 plots ($0.6 \text{ m} \times 0.6 \text{ m}$) nested within each snow fence. To increase spatial representation, three blocks were established 100 m apart with two snow fences per block.

Our measurements, including environmental variables and CO_2 flux (Section 2.1.2.) and R_{eco} $\delta^{13}\text{C}$ and $\Delta^{14}\text{C}$ (Section 2.2.1), comprised seven plots in each fences ($n = 42$) with three plots on the

control side of the fence and four plots on the soil warming side of the fence. After ~5 years, we observed heterogeneous thaw, ground subsidence, and thermokarst formation, which have created an array of TDs and soil moisture levels. We analyzed the plots as individual observations, rather than grouping plots based on assigned treatments because each plot is now unique based on where they are located in the landscape.

2.1.2 | Field measurements of environmental variables and carbon dioxide flux

All environmental variables were measured in paired plots adjacent to the R_{eco} $\delta^{13}\text{C}$ and $\Delta^{14}\text{C}$ sampling plots (see Section 2.2.1). TD was measured weekly as the distance (in cm) from the moss/surface layer to the permafrost. Soil temperature ($^{\circ}\text{C}$) was measured at 5, 10, 20, and 40 cm every half hour using type T copper-constantan thermocouples and recorded on a data logger (CR1000; Campbell Scientific). We integrated soil temperature by linearly interpolating measured temperatures from 5 to 40 cm in 5 cm increments that were averaged by plot. Soil temperature was integrated in the deep layer (>40 cm) by linearly interpolating measured temperatures from 40 cm to the permafrost (based on TD measurements) in 5 cm increments that were averaged by plot (Salmon et al., 2018). We used -0.2°C as the permafrost temperature anchor based on bore-hole measurements made annually in Eight Mile Lake (Osterkamp et al., 2009; Romanovsky et al., 2017). Soil volumetric water content (VWC; %) was recorded every half hour in each plot with TDR probes (CS 616; Campbell Scientific), and was integrated from 0 to 20 cm. Plot-level plant productivity was characterized by estimates of GPP ($\mu\text{mol C-}\text{CO}_2 \text{ m}^{-2} \text{ s}^{-1}$), obtained from automated chamber measurements of net ecosystem exchange. The plot-level values of TD, depth-integrated surface and deep soil temperatures, soil VWC, and GPP were averaged over the 30-day period that preceded each R_{eco} $\delta^{13}\text{C}$ and $\Delta^{14}\text{C}$ sampling period (Table S1). Net ecosystem exchange and R_{eco} were measured continuously during the growing season (May 1st–September 30th) using a closed-path, automated flux chamber system made from 0.6 cm thick clear polycarbonate that was designed to interface with the automated CO_2 flux system. Automated measurements were taken at each flux chamber every 1.6 h for 1.5 min using an infrared gas analyzer (LI-820, LICOR Corp.) and recorded on a data logger (CR1000; Campbell Scientific) every 2 s. See Mauritz et al. (2017) and Natali et al. (2011) for more details on the automated CO_2 flux system.

Site-level annual differences in environmental conditions were analyzed to determine if there were any extreme events or environmental anomalies during the measurement period that could indirectly influence C fluxes. Inter-annual variation in environmental conditions was determined using a linear mixed effects model, via the lme4 package (Bates et al., 2015) in R (R Development Core Team, 2015). Plot-level data were nested in corresponding snow-fence location, and both plot and snow fence were included as random effects. Environmental conditions were analyzed over

time with year included as a categorical variable and a fixed effect. Normality and homoscedasticity were visually examined using residual plots. Parameter estimates were bootstrapped to obtain 95% confidence intervals for the fixed effects, which were considered significant if the intervals did not include zero (Pinheiro & Bates, 2000).

2.2 | Isotope data

2.2.1 | Carbon isotopes of ecosystem respiration

Ecosystem respiration $\delta^{13}\text{C}$ and $\Delta^{14}\text{C}$ were collected in the field late July and early August in 2016, 2017, and 2018. Samples were collected when wind speed was $<3.1 \text{ m s}^{-1}$ to minimize atmospheric CO_2 intrusion in the chamber. Seven plots were measured in each fence ($n = 42$), including both CiPEHR and DryPEHR treatments. A 10 L dark chamber was placed on PVC collars (25.4 cm diameter \times 10 cm height) that were permanently installed 6–7 cm into the soil, and respired CO_2 from the soil and associated AG plant material was sampled. Ecosystem respiration $\delta^{13}\text{C}$ was measured from 6 to 11 a.m. (local time) to limit diurnal variation in $\delta^{13}\text{C}$ (Dudziak & Halas, 1996). Air samples were collected in Helium-flushed, septa-capped glass vials (Exetainers, Labco Limited) every 2 min, for a total of six samples per plot. Sampling was made in line with the chamber, pump, and infrared gas analyzer (Li-820; Licor) so that air circulated continuously, and the CO_2 concentration could be recorded at the time of sampling (Pries et al., 2013). Samples were shipped with CO_2 standards to correct for changes in $\delta^{13}\text{C}$ during travel and storage, and were analyzed within a week of collection at Northern Arizona University on a Thermo Finnigan Delta V Advantage continuous flow isotope ratio mass spectrometer (ThermoScientific Inc.). The Keeling method was used to obtain R_{eco} $\delta^{13}\text{C}$ based on the linear regression between $\delta^{13}\text{C}$ and $1/[\text{CO}_2]$, where the y-intercept denoted the $\delta^{13}\text{C}$ of R_{eco} (Keeling, 1958, 1961).

Ecosystem respiration $\Delta^{14}\text{C}$ was sampled after circulating the chamber headspace through soda lime for 45 min to remove atmospheric CO_2 while maintaining ambient pressure. Headspace air accumulated for 15 min and was collected in zeolite molecular sieve traps (Alltech 13X; Alltech Associates) for 15 min (Hardie et al., 2005). Traps were shipped to Northern Arizona University where they were baked at 650°C to desorb CO_2 (Bauer et al., 1992). Carbon dioxide was cryogenically purified using liquid nitrogen, and reduced to graphite by H_2 reduction with an iron catalyst on a vacuum line (Vogel et al., 1987). Graphite samples were sent to the UC Irvine W.M. Keck Carbon Cycle Accelerator Mass Spectrometry laboratory for $\Delta^{14}\text{C}$ analysis (precision $\pm 2\text{\textperthousand}$). Radiocarbon samples were analyzed with the standard oxalic acid II and corrected for mass-dependent fractionation to a common $\delta^{13}\text{C}$ value of $-25\text{\textperthousand}$. The $\Delta^{14}\text{C}$ of R_{eco} was estimated using a two-pool mixing model to account for any atmospheric contamination (Stuiver & Polach, 1977; Trumbore, Sierra, et al., 2016; Trumbore, Xu, et al., 2016).

2.2.2 | Carbon isotope measurements to inform AG and BG plant end-members

Aboveground and BG plant tissues were harvested in July 2018 using a serrated bread knife to cut a 20 cm^3 block of tundra from destructive plots ($n = 12$) adjacent to environmental and R_{eco} $\delta^{13}\text{C}$ and $\Delta^{14}\text{C}$ plots. All AG live plant materials, including moss and lichen, were clipped and placed into foil-covered 1 L Mason jars within 5 min of collection. All live roots and rhizomes ($>1 \text{ mm}$ in diameter) were collected from the soil, rinsed twice with deionized water to remove soil particles, shaken to remove excess moisture, and placed in separate foil-covered Mason jars within 30 min of collection. The headspace air in each jar was circulated through soda lime for 5 min at a flow rate of 1 L min^{-1} to remove atmospheric CO_2 . Delta $\delta^{13}\text{C}$ was sampled by incubating AG and BG samples for 10 min and collecting headspace air into CO_2 -free Exetainers. Delta $\Delta^{14}\text{C}$ was sampled by incubating AG and BG plant tissue for 4 h and collecting headspace air in zeolite molecular sieve traps for 15 min (Hardie et al., 2005; Pries et al., 2016). The $\delta^{13}\text{C}$ and $\Delta^{14}\text{C}$ sample preparation and analyses were conducted as described in Section 2.2.1.

2.2.3 | Carbon isotope measurements to inform soil end-members

Six soil cores were collected in May 2017 to measure the $\delta^{13}\text{C}$ and $\Delta^{14}\text{C}$ of soil-respired CO_2 . The seasonally thawed soil was cut using a serrated knife, and the underlying frozen soil was cored using a SIPRE coring auger (7.5 cm diameter) to the depth at which the corer hit rocks (85–102 cm). In the laboratory, the surface vegetation was clipped off, and cores were sectioned to 15 cm at the surface and 10 cm increments thereafter (0–15, 15–25 cm, etc.) to the end of the core, and each soil section was placed in separate 1 L Mason jars. Roots $>1 \text{ mm}$ in diameter were removed from surface soil (0–25 cm) before the incubation. Soils were pre-incubated for 10 days at 15°C to ensure that the labile, recently fixed C from roots did not contribute to soil end-member analysis, and so that microbial turnover was stabilized after thaw (Pries et al., 2013; Schuur & Trumbore, 2006). After the pre-incubation period, soils were incubated at field moisture at 15°C, and CO_2 flux was measured on a Licor-820 infrared gas analyzer in a closed-loop automated soil incubation system immediately before and after isotope sampling (see Bracho et al., 2016 for details on the automated incubation system). For isotope collection, the headspace air of each jar was circulated through soda lime for 5 minutes to remove atmospheric CO_2 . Jars were sealed and incubated at 15°C until 0.5–1.5 mg CO_2 -C was accumulated in the headspace, based on the first flux measurement. Headspace air was collected in zeolite molecular sieve traps by circulating air for 5 min at a flow rate of 1 L min^{-1} . The $\Delta^{14}\text{C}$ sample preparation and analysis was conducted as described for R_{eco} in Section 2.2.1. After purification, a subsample of CO_2 was collected in Helium-flushed Exetainers for $\delta^{13}\text{C}$ analysis.

Soil respiration was separated into two sources: YS from the surface layer (0–25 cm) and old soil (OS) from deeper layers (25–102 cm). Surface soil layers have positive $\Delta^{14}\text{C}$ values that contain bomb-produced radiocarbon (post-1950), and indicate soil that is “younger” relative to the entire soil profile. Delta ^{14}C values become more negative with depth, indicating the bulk of soil C has resided in the soil long enough for radioactive decay to occur (i.e., “old” soil; Trumbore, 2000). The $\delta^{13}\text{C}$ values were corrected for the higher incubation temperature because $\delta^{13}\text{C}$ becomes depleted by 0.16‰ for each 1°C increase in temperature (Dorrepaal et al., 2009; Pries et al., 2013). Since the ^{14}C isotopic composition of CO_2 is corrected for fractionation during data processing based on the $\delta^{13}\text{C}$, we did not apply a temperature correction to the $\Delta^{14}\text{C}$ of soil respiration.

We combined the isotopic signatures of each incubated depth increment into a YS (0–25 cm) and OS (>25 cm) end-member for each core. We weighted each depth increment’s contribution to each end-member based on (1) the relative amount of soil mass, (2) the relative CO_2 flux on a per gram dry soil basis, and (3) the average field soil temperature at each depth (Schuur & Trumbore, 2006). The temperature correction was based on measured field temperatures that were averaged for the 2-week period preceding the R_{eco} measurements, and a temperature sensitivity of SOM microbial decomposition using a Q_{10} of 2.6 based on Bracho et al. (2016) (Table S2).

2.3 | Data analysis and isotope mixing model

2.3.1 | Regression model for R_{eco} $\delta^{13}\text{C}$ and $\Delta^{14}\text{C}$

A Bayesian linear regression model was used to evaluate the environmental drivers of R_{eco} $\delta^{13}\text{C}$ and $\Delta^{14}\text{C}$ with the goal of informing the Bayesian mixing model (see Section 2.3.2). Covariates included TD, GPP, VWC (0–20 cm), depth-integrated surface (T_{surface} ; 0–40 cm) and deep (T_{deep} ; 40 cm to permafrost) soil temperatures, and all two-way interactions, minus TD and soil temperature interactions because TD, T_{surface} , and T_{deep} covary. Mean-centered covariates were used in the regression by subtracting the mean value of each covariate from individual values.

To arrive at the most parsimonious model that could also help inform the Bayesian mixing model, model selection was conducted by removing one covariate at a time, starting with the interaction terms, and comparing it to the original full model. The final covariates and interactions included in the regression model, Equation (2), were determined by comparing changes in the deviance information criterion, effective number of parameters (pD; Spiegelhalter et al., 2002), the sum of the squared difference (D_{sum}) between the observed and predicted $\delta^{13}\text{C}$ and $\Delta^{14}\text{C}$ data, and the adjusted R^2 from regressions of observed vs. predicted values (Table S3).

For observation i ($i = 1, 2, \dots, 252$; based on 42 plots \times 2 isotopes \times 3 years), we assumed that the observed plot-level R_{eco} $\delta^{13}\text{C}$ and $\Delta^{14}\text{C}$ data followed a normal distribution with mean, μ :

$$\text{Iso}_i \sim \text{Normal}(\mu_{y(i), p(i), \text{Iso}}, \sigma_{\text{Iso}}^2), \quad (1)$$

where $y(i)$ and $p(i)$ denote year ($y = 1, 2, 3$; for 2016, 2017, 2018) and plot ($p = 1, 2, \dots, 42$) associated with observation i . Note that the mean, $\mu_{y,p,\text{Iso}}$, and SD term, σ_{Iso} , both vary by isotope ($\delta^{13}\text{C}$ and $\Delta^{14}\text{C}$), as indicated by the Iso subscript. Our final model resulted in the following regression model for $\mu_{y,p,\text{Iso}}$:

$$\begin{aligned} \mu_{y,p,\text{Iso}} = & \beta_{0,y,\text{Iso}} + \sum_{k=1}^5 \beta_{k,y,\text{Iso}} \cdot X_{k,y,p} + \beta_{6,y,\text{Iso}} \cdot \text{GPP}_{y,p} \cdot \text{VWC}_{y,p} \\ & + \beta_{7,y,\text{Iso}} \cdot \text{GPP}_{y,p} \cdot T_{\text{surface},y,p} + \beta_{8,y,\text{Iso}} \cdot \text{GPP}_{y,p} \cdot \text{TD}_{y,p} \\ & + \beta_{9,y,\text{Iso}} \cdot \text{VWC}_{y,p} \cdot \text{TD}_{y,p}, \end{aligned} \quad (2)$$

where X indicates individual covariates, where $k = 1, 2, \dots, 5$ denotes TD, GPP, VWC, T_{surface} , and T_{deep} , respectively. All β parameters vary by year y and isotope Iso , and all covariates vary by year y and plot p . To complete the model, we specified relatively non-informative priors for the β parameters and the standard deviation term σ_{Iso} , such that $\beta_{k,y,\text{Iso}} \sim \text{Normal}(0, 100,000)$ and $\sigma_{\text{Iso}} \sim \text{Uniform}(0, 100)$.

2.3.2 | Bayesian dual-isotope mixing model

Our analysis included (1) end-member models based on measured $\delta^{13}\text{C}$ and $\Delta^{14}\text{C}$ of plant and soil incubations, (2) a dual-isotope mixing model to partition R_{eco} , and (3) a generalized linear regression used to determine environmental drivers governing the relative contributions of AG and BG plant respiration, and young (YS) and old (OS) soil respiration to R_{eco} . These models were implemented in a hierarchical Bayesian framework (Gelman et al., 2014) to allow for the propagation of both the natural variability in each observed source end-member (i.e., AG, BG, YS, and OS) and parameter uncertainty (Ogle & Pendall, 2015; Ogle et al., 2014).

End-member models

The $\delta^{13}\text{C}$ and $\Delta^{14}\text{C}$ of each plant end-member incubation replicate r ($\delta^{13}\text{C}$, $n = 12$; $\Delta^{14}\text{C}$, $n = 6$) and the flux-weighted $\delta^{13}\text{C}$ and $\Delta^{14}\text{C}$ of each soil end-member incubation replicate r ($\delta^{13}\text{C}$, $n = 6$; $\Delta^{14}\text{C}$, $n = 6$) were each assumed to follow a normal distribution:

$$\text{EM}_{r,\text{Iso}} \sim \text{Normal}(\mu_{\text{EM},\text{Iso}}, \sigma_{\text{EM},\text{Iso}}^2), \quad (3)$$

where EM denotes the end-member of interest (AG, BG, YS, or OS), and Iso refers to the isotope (again, $\delta^{13}\text{C}$ or $\Delta^{14}\text{C}$). The predicted mean value ($\mu_{\text{EM},\text{Iso}}$) varies by each end-member and isotope type, as does the SD term ($\sigma_{\text{EM},\text{Iso}}$) that describes variation among replicates. The end-member models were modularized so that the dual-isotope mixing model did not feedback to affect each source end-member estimate, $\mu_{\text{EM},\text{Iso}}$, thus allowing only the observed end-member data to inform $\mu_{\text{EM},\text{Iso}}$ (Ogle & Pendall, 2015). We assigned relatively non-informative, vague normal priors to $\mu_{\text{EM},\text{Iso}}$ and wide uniform priors to the standard deviations, $\sigma_{\text{EM},\text{Iso}}$. These latent or predicted end-members, $\mu_{\text{EM},\text{Iso}}$, were subsequently used in the mixing model (see Equation 4).

Dual-isotope mixing model

To estimate plot-level source contributions to R_{eco} , a dual-isotope mixing model was implemented using the same data and normal likelihood as described in Equation (1). However, in the mixing model, the predicted mean $R_{\text{eco}} \delta^{13}\text{C}$ and $\Delta^{14}\text{C}$ values, denoted by $\mu_{y,p,\text{Iso}}$, are defined as the sum of the proportional contribution of each source. The plot-level proportional contribution p_{EM} of each source (EM = AG, BG, YS, or OS) varied by year y and plot p , and was multiplied by its corresponding end-member isotope value, $\mu_{\text{EM},\text{Iso}}$, obtained from the end-member models in Equation (3) such that:

$$\mu_{y,p,\text{Iso}} = p_{\text{AG},y,p} \cdot \mu_{\text{AG},\text{Iso}} + p_{\text{BG},y,p} \cdot \mu_{\text{BG},\text{Iso}} + p_{\text{YS},y,p} \cdot \mu_{\text{YS},\text{Iso}} + p_{\text{OS},y,p} \cdot \mu_{\text{OS},\text{Iso}}. \quad (4)$$

Note that unlike traditional, non-Bayesian mixing models, the end-member values are typically provided as observed data, but here, $\mu_{\text{EM},\text{Iso}}$, is treated as an unknown, stochastic parameters, and uncertainty in the end-member values is thus propagated to the mixing model in Equation (4).

Linear regression model

We incorporated the effects of plant productivity (via GPP) and the potentially important environmental drivers to help constrain and understand drivers of the relative contributions of plant and soil respiration to R_{eco} . The relative contributions of the plant sources were directly constrained by the measured plot-level GPP values since we expected that the proportion of R_{eco} from plant (both AG and BG) respiration, p_{Plant} , to be related to measured plant activity captured by GPP:

$$p_{\text{Plant},y,p} = p \cdot \text{GPP}_{y,p}, \quad (5)$$

where the year- and plot-specific $p_{\text{Plant},y,p}$ contribution is expected to be proportional to GPP with p being the constant of proportionality, which is given a uniform prior that ensures that $p_{\text{Plant},y,p}$ is constrained between 0 and 1. From a simple mass-balance equation, we derived the models for the AG and BG contributions, $p_{\text{AG},y,p}$ and $p_{\text{BG},y,p}$, by partitioning the total plant contribution into these two plant sources:

$$\begin{aligned} p_{\text{AG},y,p} &= p_{\text{Plant},y,p} \cdot p_{\text{AG}|\text{Plant},y,p} \\ p_{\text{BG},y,p} &= p_{\text{Plant},y,p} \cdot (1 - p_{\text{AG}|\text{Plant},y,p}), \end{aligned} \quad (6)$$

where $p_{\text{AG}|\text{Plant},y,p}$ is the proportional contribution of AG respiration to the total plant respiration.

Since the source proportional contributions to R_{eco} must add to 1, the total soil contribution, p_{Soil} , is given by:

$$p_{\text{Soil},y,p} = 1 - p_{\text{Plant},y,p}. \quad (7)$$

As in Equation (6), the proportional contributions of OS and YS, $p_{\text{OS},y,p}$ and $p_{\text{YS},y,p}$, are given by:

$$\begin{aligned} p_{\text{OS},y,p} &= p_{\text{Soil},y,p} \cdot p_{\text{OS}|\text{Soil},y,p} \\ p_{\text{YS},y,p} &= p_{\text{Soil},y,p} \cdot (1 - p_{\text{OS}|\text{Soil},y,p}). \end{aligned} \quad (8)$$

And, $p_{\text{OS}|\text{Soil},y,p}$ is the proportional contribution of OS respiration to the total soil respiration.

The conditional proportional contribution of AG respiration, $p_{\text{AG}|\text{Plant},y,p}$ Equation (6), and the conditional proportional contribution of OS respiration, $p_{\text{OS}|\text{Soil},y,p}$ Equation (8), relative to total plant respiration and total soil respiration, were modeled on a logit scale, thus constraining $p_{\text{AG}|\text{Plant},y,p}$ and $p_{\text{OS}|\text{Soil},y,p}$ to the (0, 1) interval. To account for plot and year random effects, the logit-scale contributions were assumed to come from a normal distribution:

$$\begin{aligned} \text{logit}(p_{\text{AG}|\text{Plant},y,p}) &\sim \text{Normal}(\mu_{\text{AG}|\text{Plant},y,p}, \sigma_{\text{AG}|\text{Plant}}^2) \\ \text{logit}(p_{\text{OS}|\text{Soil},y,p}) &\sim \text{Normal}(\mu_{\text{OS}|\text{Soil},y,p}, \sigma_{\text{OS}|\text{Soil}}^2), \end{aligned} \quad (9)$$

where the SD terms, $\sigma_{\text{AG}|\text{Plant}}$, and $\sigma_{\text{OS}|\text{Soil}}$, were assigned relatively non-informative priors, Uniform(0, 100).

We modeled the logit-scale means, $\mu_{\text{AG}|\text{Plant},y,p}$ and $\mu_{\text{OS}|\text{Soil},y,p}$ in Equation (9), as a linear function of GPP and environmental drivers by applying the general form of the linear regression arrived at in Equation (2):

$$\begin{aligned} \mu_{\text{AG}|\text{Plant},y,p} &= \alpha_{0,y} + \sum_{k=1}^5 \alpha_{k,y} \cdot X_{k,y,p} + \alpha_{6,y} \cdot \text{GPP}_{y,p} \cdot \text{VWC}_{y,p} + \alpha_{7,y} \cdot \text{GPP}_{y,p} \\ &\quad \times T_{\text{surface},y,p} + \alpha_{8,y} \cdot \text{GPP}_{y,p} \cdot \text{TD}_{y,p} + \alpha_{9,y} \cdot \text{VWC}_{y,p} \cdot \text{TD}_{y,p} \\ \mu_{\text{OS}|\text{Soil},y,p} &= \beta_{0,y} + \sum_{k=1}^5 \beta_{k,y} \cdot X_{k,y,p} + \beta_{6,y} \cdot \text{GPP}_{y,p} \cdot \text{VWC}_{y,p} + \beta_{7,y} \cdot \text{GPP}_{y,p} \\ &\quad \times T_{\text{surface},y,p} + \beta_{8,y} \cdot \text{GPP}_{y,p} \cdot \text{TD}_{y,p} + \beta_{9,y} \cdot \text{VWC}_{y,p} \cdot \text{TD}_{y,p}, \end{aligned} \quad (10)$$

where the $\alpha_{k,y}$ and $\beta_{k,y}$ parameters ($k = 1, 2, 3, \dots, 9$) varied by year y , and all environmental covariates varied by year y and plot p (see Equation 2 for additional details about notation). We specified relatively non-informative priors for the α and β terms, with $\alpha_{k,y}$ and $\beta_{k,y}$ both being assigned Normal(0, 1000) priors. While this prior may appear tighter than the prior used for β in Equation (2), because α and β enter into a logit-scale mean model in Equation (10), this prior is actually quite vague.

2.3.3 | Total respiration of old soil C model

Total respiration from old soil C was estimated by multiplying the cumulative growing season R_{eco} flux (Section 2.1.2), in g CO₂-C m⁻², by the plot-level proportional contributions of old soil respiration, $p_{\text{Soil},y,p}$ from Equation (7). We then modeled total respiration from old soil C as a linear function of GPP and environmental drivers by applying the general form of the linear regression arrived at in Equations (2) and (10). Though we expect that the proportion of R_{eco} from old soil C to vary throughout the growing season, this is a first-order estimate of the magnitude of old soil C loss between the sampled years that allowed us to elucidate which covariates contributed to the greatest magnitude of old soil C release at the ecosystem scale:

$$\mu_{Ros} = \beta_{0,y} + \sum_{k=1}^5 \beta_{k,y} \cdot X_{k,y,p} + \beta_{6,y} \cdot GPP_{y,p} \cdot VWC_{y,p} + \beta_{7,y} \cdot GPP_{y,p} \cdot T_{surface,y,p} \\ + \beta_{8,y} \cdot GPP_{y,p} \cdot TD_{y,p} + \beta_{9,y} \cdot VWC_{y,p} \cdot TD_{y,p}, \quad (11)$$

where the $\beta_{k,y}$ parameters ($k = 1, 2, 3, \dots, 9$) varied by year y , and all environmental covariates varied by year y and plot p (see Equation 2 for additional details about notation). We specified relatively non-informative priors for the β parameters and the SD term σ such that $\beta_{k,y} \sim \text{Normal}(0, 100,000)$ and $\sigma \sim \text{Uniform}(0, 100)$.

2.4 | Model interpretation and implementation

The models described by Equations (1)–(11) were implemented in OpenBUGS via the R2Openbugs function in R (Sturtz et al., 2005). We used OpenBUGS because it allowed us to modularize the end-member models (Equation 3) using the cut function (Lunn et al., 2009) such that the isotope mixing model and associated data on R_{eco} $\delta^{13}\text{C}$ and $\Delta^{14}\text{C}$ did not feedback to influence the estimates of the end-members, $\mu_{EM,\text{iso}}$ (Ogle et al., 2013). The regression model for R_{eco} $\delta^{13}\text{C}$ and $\Delta^{14}\text{C}$, the Bayesian dual-isotope mixing model, and the total respiration of old soil C model were implemented with three parallel Markov chain Monte Carlo sequences with 1×10^6 iterations to ensure convergence was achieved, as measured by the Gelman–Rubin statistic (Gelman & Rubin, 1992). We thinned the sequences every 50 iterations to reduce auto-correlation within each chain and storage requirements, resulting in a posterior sample size of 20,000 iterations for each parameter. Model fit was assessed by comparing observed vs. predicted R_{eco} $\delta^{13}\text{C}$ and $\Delta^{14}\text{C}$ values and computing the adjusted R^2 values (Gelman et al., 2004). The marginal effects of significant two-way interactions from the regression model for R_{eco} $\delta^{13}\text{C}$ and $\Delta^{14}\text{C}$ (Equation 2) and the total respiration of old soil C model (Equation 11) were plotted using the packages sjPlot and sjmisc in R (Lüdecke, 2018).

All parameters of interest were summarized by their posterior means and 95% credible interval (CI), defined by the 2.5th and 97.5th percentiles of the posterior distributions. Parameters were considered significant if the 95% CI did not overlap zero. We computed posterior distributions for site-level proportional contribution of each source by averaging the plot-level proportions by year and source, from Equations (6) and (8). The posterior distributions of each annual, site-level proportional source contribution to R_{eco} were deemed significantly different from each other if the 95% CI for one group level (e.g., AG in 2016) did not overlap the mean of another group level (e.g., AG in 2017).

3 | RESULTS

3.1 | Ecosystem respired $\delta^{13}\text{C}$ and $\Delta^{14}\text{C}$ and site environmental conditions

Ecosystem respired $\delta^{13}\text{C}$ varied from $-25.8\text{\textperthousand}$ to $-17.6\text{\textperthousand}$ (mean = $-22.6\text{\textperthousand}$; Figure 1a; Table S4), and was significantly different across years. Ecosystem respired $\Delta^{14}\text{C}$ ranged from $-242\text{\textperthousand}$ to $43\text{\textperthousand}$ across all plots and years (mean = $18\text{\textperthousand}$; Figure 1b; Table

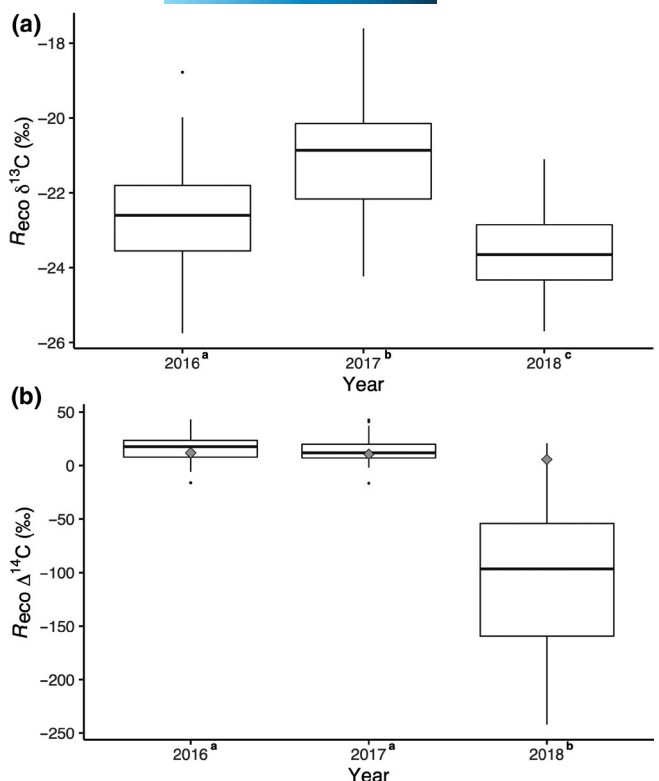


FIGURE 1 Ecosystem respiration (R_{eco}) isotopic compositions as described by (a) $\delta^{13}\text{C}$ and (b) $\Delta^{14}\text{C}$ measured at the plot level in 2016, 2017, and 2018. Values are represented in permil notation (‰) and show the range of values measured each year, summarized among plots each year with the sample median, interquartile range (IQR = 25th–75th percentile, Q1–Q3), minimum (Q1 – 1.5 × IQR) and maximum (Q3 + 1.5 × IQR), the boxes, the whiskers, and the small black circle symbols, respectively. The gray rhombus shape (b) represent atmospheric $\Delta^{14}\text{C}$ of each year. The $\Delta^{14}\text{C}$ values above 0‰ represent bomb enrichment of atmospheric ^{14}C in the late 1950s (b). The y scale differs between (a) and (b). Letters in the x-axis denote significant differences among years for each isotope

S4). Mean measured $R_{\text{eco}} \Delta^{14}\text{C}$ did not significantly differ between 2016 and 2017, and predominantly reflected respiration of enriched “bomb peak” ^{14}C (Figure 1b; Table S4). In 2018, the mean $R_{\text{eco}} \Delta^{14}\text{C}$ was $-114\text{\textperthousand}$, which was significantly more depleted in ^{14}C relative to the previous 2 years and lower than atmospheric $\Delta^{14}\text{C}$ concentrations in 2016–2018 (Figure 1b, Table S4), predominantly reflecting respiration of old C that had undergone significant ^{14}C radioactive decay.

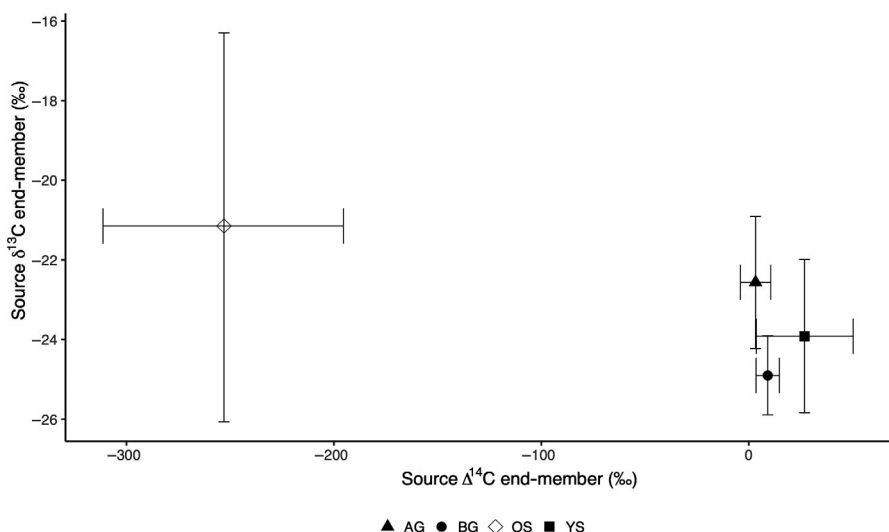
The much lower mean $R_{\text{eco}} \Delta^{14}\text{C}$ measured in 2018 prompted the question of whether site-level environmental conditions were significantly different in 2018 relative to 2016 and 2017. We found that in 2016, soil VWC, T_{surface} , and T_{deep} were significantly higher relative to 2017 and 2018 (Table 1). In 2017, GPP and R_{eco} fluxes were significantly lower, and soil was significantly colder at depth with a shallower TD relative to 2016 and 2018 (Table 1). In 2018, the soil was significantly drier compared to 2016 and 2017 (Table 1).

3.2 | Source end-member $\delta^{13}\text{C}$ and $\Delta^{14}\text{C}$

The respiration $\delta^{13}\text{C}$ and $\Delta^{14}\text{C}$ source end-members, $\mu_{\text{EM},\text{iso}}$ in Equation (3), differed significantly among sources (Figure 2). The posterior means of AG and BG $\delta^{13}\text{C}$ averaged $-22.6\text{\textperthousand}$ and $-24.9\text{\textperthousand}$, respectively, with BG being significantly more depleted in ^{13}C . The respiration

TABLE 1 Environmental variables and gross primary productivity (GPP) for the 30-day period before R_{eco} $\delta^{13}\text{C}$ and $\Delta^{14}\text{C}$ sampling, and growing season (May 1st–September 30th) cumulative R_{eco} fluxes ($\text{g CO}_2\text{-C m}^{-2}$) from 2016 to 2018. Mean values are reported, along with the lower (2.5%) and upper (97.5%) limits of the 95% confidence interval. Letters in the "Year" column represent significant differences between years for each variable

Variable	Year	Mean	2.5% Lower limit	97.5% Upper limit
Volumetric water content (VWC, 0–20 cm; %)	2016 ^a	59.1	54.9	63.2
	2017 ^b	53.2	51.4	55.0
	2018 ^c	47.6	45.9	49.3
Thaw depth (TD, cm)	2016 ^a	78.9	74.1	83.7
	2017 ^b	57.5	53.9	61.1
	2018 ^a	77.3	73.7	80.9
Surface soil temperature (T_{surface} , 0–40 cm; $^{\circ}\text{C}$)	2016 ^a	6.0	5.6	6.4
	2017 ^b	5.3	5.0	5.7
	2018 ^b	5.5	5.1	5.8
Deep soil temperature (T_{deep} , 40 cm-permafrost; $^{\circ}\text{C}$)	2016 ^a	1.3	1.0	1.6
	2017 ^c	0.5	0.3	0.7
	2018 ^b	1.0	0.8	1.2
Gross primary productivity (GPP, $\mu\text{mol C-CO}_2\text{ m}^{-2}\text{ s}^{-1}$)	2016 ^a	5.4	4.6	6.3
	2017 ^b	6.6	6.3	7.0
	2018 ^a	5.6	5.2	6.0
Ecosystem respiration (R_{eco} ; $\text{g C-CO}_2\text{ m}^{-2}$)	2016 ^a	416.6	357.0	476.4
	2017 ^b	295.8	262.7	328.8
	2018 ^a	399.1	366.7	430.7



$\delta^{13}\text{C}$ of YS was similar to BG and averaged $-23.9\text{\textperthousand}$, while the $\delta^{13}\text{C}$ of OS ranged from -26.1 to $-16.3\text{\textperthousand}$ (95% CI) and overlapped the posterior means of all other source $\delta^{13}\text{C}$ end-members (Figure 2). Conversely, the respiration $\Delta^{14}\text{C}$ of OS was significantly more depleted in ^{14}C than all other sources, and averaged $-253\text{\textperthousand}$ (Figure 2). While the 95% CI for OS $\Delta^{14}\text{C}$ was also wide, compared to the $\Delta^{14}\text{C}$ 95% CI of the other sources, it did not overlap with the posterior means of other sources. The mean plant respiration $\Delta^{14}\text{C}$ was 3\textperthousand and 9\textperthousand for AG and BG, respectively, and were not significantly different from one another, but were significantly less enriched in ^{14}C than the respiration $\Delta^{14}\text{C}$ of YS, which averaged $27\text{\textperthousand}$ (Figure 2). While $\Delta^{14}\text{C}$ clearly separated the OS end-member from the other three end-members, $\Delta^{14}\text{C}$ and $\delta^{13}\text{C}$ were both required to distinguish among the younger end-members (AG, BG, and YS).

3.3 | Model fit

We evaluated the model fit of both the regression model, Equation (2), and the dual-isotope mixing model, Equation (4) and linked equations that simultaneously modeled variation in the measured R_{eco} $\delta^{13}\text{C}$ and $\Delta^{14}\text{C}$. Model fit was quantified with a regression of predicted vs. observed plot-level R_{eco} $\delta^{13}\text{C}$ and $\Delta^{14}\text{C}$ values. The regression model yielded an R^2 of 0.62 (Figure S1a) and 0.84 (Figure S1b) for $\delta^{13}\text{C}$ and $\Delta^{14}\text{C}$, respectively. The dual-isotope mixing model yielded an R^2 of 0.04 ($p = 0.02$, Figure S2a) and 0.86 ($p < 0.001$; Figure S2b) for $\delta^{13}\text{C}$ and $\Delta^{14}\text{C}$, respectively.

The $\Delta^{14}\text{C}$ data provided most of the information for the dual-isotope mixing model. We attempted to improve the mixing model by constraining the $\delta^{13}\text{C}$ data to only resolving plant contributions (Equations 5 and 6) since the $\delta^{13}\text{C}$ end-members for AG and BG were significantly different from one another (Figure 2). However, this modification to the model did not improve the fit for the $\delta^{13}\text{C}$ data ($R^2 = 0.002$), and only slightly improved the fit for the $\Delta^{14}\text{C}$ data ($R^2 = 0.90$); therefore, we used both isotope data to inform plant and soil contributions in the mixing model.

FIGURE 2 Posterior means and 95% credible intervals (CI) for the $\delta^{13}\text{C}$ (‰) and $\Delta^{14}\text{C}$ (‰) of aboveground (AG), belowground (BG), old soil (OS), and young soil (YS) end-members (Equation 3). Source endmembers were considered statistically significant if the posterior mean of one source was not contained within the CI of another source

3.4 | Drivers of R_{eco} $\delta^{13}\text{C}$ and $\Delta^{14}\text{C}$

Overall, GPP and environmental conditions explained variation in R_{eco} $\delta^{13}\text{C}$ in the wet years (2016 and 2017), but not in the dry year (2018). For example, TD and the interaction between TD and VWC were significant drivers of R_{eco} $\delta^{13}\text{C}$ in 2016 and 2017 (Table S5; Figure S3a), but not in 2018. TD had contrasting effects on R_{eco} $\delta^{13}\text{C}$ in 2016 and 2017, where deeper TD decreased R_{eco} $\delta^{13}\text{C}$ in 2016, but increased R_{eco} $\delta^{13}\text{C}$ in 2017. The positive TD \times VWC interaction effect for R_{eco} $\delta^{13}\text{C}$ indicates that R_{eco} $\delta^{13}\text{C}$ was more positive (i.e., more enriched in ^{13}C) in deeply thawed plots that were wetter. In 2016, GPP was significant and associated with more enriched R_{eco} $\delta^{13}\text{C}$ values (Table S5; Figure S3a).

Conversely, GPP and environmental conditions explained variation in R_{eco} $\Delta^{14}\text{C}$ in the dry year, but not in the wet years. Variation in R_{eco} $\Delta^{14}\text{C}$ in 2018 was associated with the main effects of T_{surface} and T_{deep} , and the interactions between GPP and the covariates VWC, T_{surface} , and TD (Table S5; Figure S3b), with no significant covariate effects in 2016 and 2017. In 2018, R_{eco} $\Delta^{14}\text{C}$ decreased with warmer T_{surface} and increased with warmer T_{deep} , which was opposite to what we expected (Table S5; Figure S3b). As main effects, GPP, VWC, and TD were not significant predictors by themselves, but interacted to affect R_{eco} $\Delta^{14}\text{C}$. The significant GPP \times VWC and GPP \times T_{surface} interactions indicate that R_{eco} $\Delta^{14}\text{C}$ become increasingly more enriched (i.e., younger C) in plots with high GPP that were wetter (Figure 3a; Table S5; Figure S3b) and warmer at the surface (Figure 3b; Table S5; Figure S3b). Also surprising was the significant interaction between GPP and TD, showing that regardless of GPP, plots with shallower TD induced respiration of more depleted R_{eco} $\Delta^{14}\text{C}$ (i.e., older C), whereas deeper TD had higher R_{eco} $\Delta^{14}\text{C}$ (Figure 3c; Table S5; Figure S3b).

3.5 | Proportional source contributions to R_{eco}

The proportional source contributions to R_{eco} differed among years (Figure 4). Based on the posterior mean and 95% CI estimates for p_{AG} , p_{BG} , p_{OS} , and p_{YS} , the proportional source contributions were similar in 2016 and 2017, but changed in 2018. In 2016 and 2017, YS and AG were the dominant sources, contributing 56.7% (CI: 42.4, 71.0) and 38.3% (CI: 20.4, 54.3) to R_{eco} in 2016, and 45.5% (CI: 28.1, 63.2) and 49.5% (CI: 31.4, 67.4) to R_{eco} in 2017 (Figure 4). In 2018, there was a shift in the main source contributions, where OS and BG respiration contributed 38.8% (CI: 25.2, 52.0) and 37.6% (CI: 17.6, 54.8) to R_{eco} , and were significantly higher than YS (17.0%, CI: 6.8, 28.9) and AG respiration (6.6%, CI: 0.0, 24.0; Figure 4). In the dry year, the shift in the proportional contribution of OS to R_{eco} represents a 30-fold increase compared to the average p_{OS} of wet years.

3.6 | Drivers of old soil C respiration

The magnitude of growing season OS respiration, based on plot-level proportions of OS multiplied by the plot-level cumulative

Marginal effects of interaction terms on R_{eco} $\Delta^{14}\text{C}$

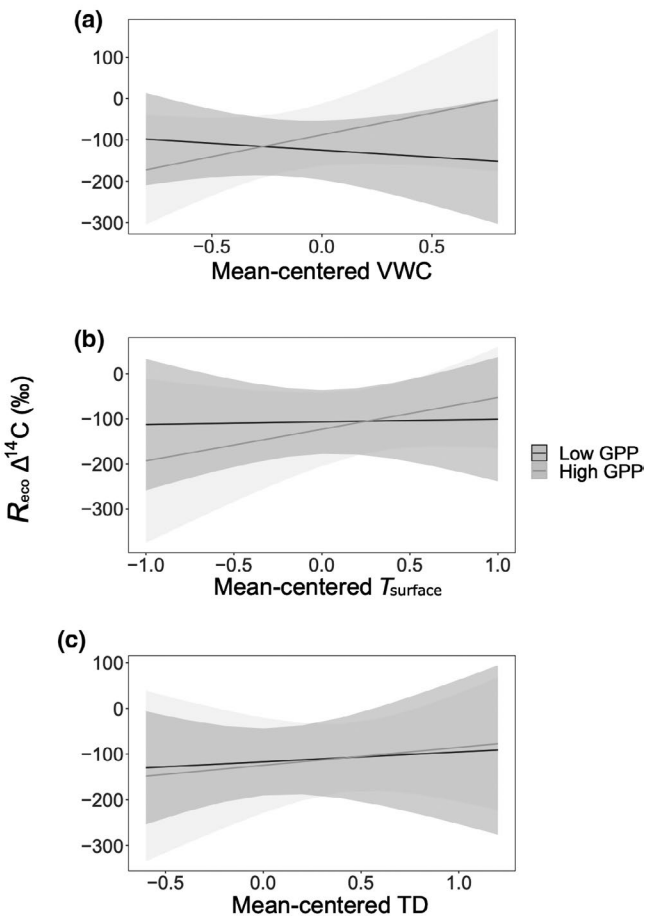


FIGURE 3 Marginal effects of the interaction terms (a) gross primary productivity (GPP) and volumetric water content (VWC), (b) GPP and T_{surface} , and (c) GPP and thaw depth (TD) on R_{eco} $\Delta^{14}\text{C}$ (%) in 2018. The variables VWC, T_{surface} , and TD are mean-centered and for the continuous variable, GPP, the minimum and maximum values are chosen as the grouping levels (i.e., high and low GPP)

growing season R_{eco} (g C m^{-2}), was significantly higher in 2018 than 2016 and 2017 (Figure 5). In 2016 and 2017, the growing season OS loss was 0.98 g C m^{-2} (0.01, 6.80) and 3.58 g C m^{-2} (0.00, 14.00). In 2018, the average growing season OS loss increased to $151.51 \text{ g C m}^{-2}$ (97.51, 204.30), representing a 65-fold increase in the magnitude of growing season OS loss relative to wet years.

The variation in the growing season OS respiration in 2018 was explained by the main effect T_{deep} , and the GPP \times VWC interaction (Figure S4). There were no significant covariate effects on growing season OS respiration in 2016 or 2017. In 2018, warmer T_{deep} resulted in a decrease in OS loss, which was similar to the temperature effect on R_{eco} $\Delta^{14}\text{C}$. At the same time, plots with warmer T_{deep} tended to also have greater soil VWC (2018 $R^2 = 0.3$, $p < 0.001$; Figure 6), which may have suppressed OS respiration, thus counteracting the expected temperature response on old soil C loss. Soil VWC also interacted with GPP to affect growing season OS respiration in a similar way it affected R_{eco} $\Delta^{14}\text{C}$; there was a significantly

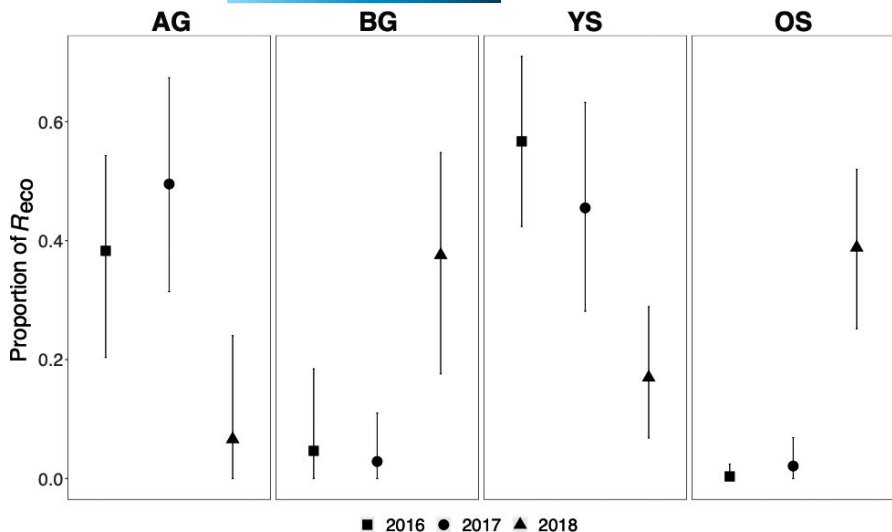


FIGURE 4 Posterior means and 95% credible intervals (CI) for the proportional contributions of aboveground (AG), belowground (BG), young soil (YS), and old soil (OS) respiration to ecosystem respiration (R_{eco}) for 2016, 2017, and 2018. These year-specific contributions were obtained by averaging the plot-level contributions ($p_{\text{AG}_{y,p}}, p_{\text{BG}_{y,p}}, p_{\text{YS}_{y,p}}, p_{\text{OS}_{y,p}}$; Equation 4) across all plots p for each year y . Source contributions were considered significantly different if the posterior mean of one group (given by source type and year) was not contained within the CI of another group

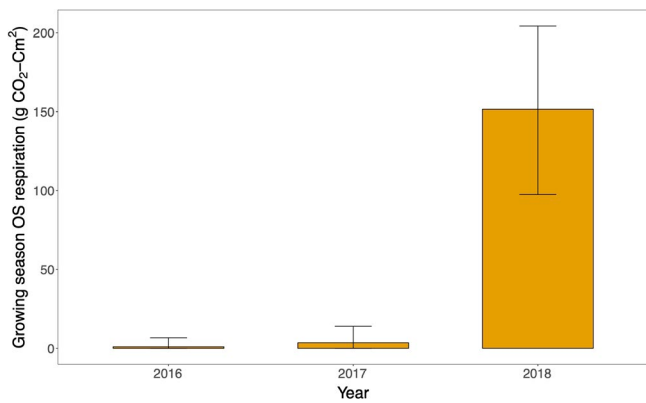


FIGURE 5 Posterior means and 95% credible intervals (CI) for growing season old soil C respiration ($\text{g CO}_2\text{-C m}^{-2}$) based on plot-level proportional contributions of OS respiration ($p_{\text{OS}_{y,p}}$, Equation 2) multiplied by the plot-level cumulative growing season R_{eco} ($\text{g CO}_2\text{-C m}^{-2}$), averaged by year [Colour figure can be viewed at wileyonlinelibrary.com]

negative effect on OS loss in plots with high GPP that were also wetter (Figure 7; Figure S4).

4 | DISCUSSION

Enhanced R_{eco} in tundra undergoing permafrost thaw is likely to be a positive feedback to the atmosphere from an increase in old soil C loss (Czimczik & Welker, 2010; Dorrepaal et al., 2009; Nowinski et al., 2010; Pries et al., 2013, 2016; Schuur et al., 2009). Warmer soil temperature has been shown to increase the proportion of old soil C to R_{eco} (Pries et al., 2013, 2016; Schuur et al., 2009); however, our study highlights that long-term experimental permafrost warming can introduce a soil hydrology component that, along with temperature, affect old soil C loss. In 2018, old soil C loss was suppressed in plots with warmer deep soil temperatures, as they tended to be wetter from increased soil subsidence in thermokarst features across the landscape. Additionally, the surprisingly large

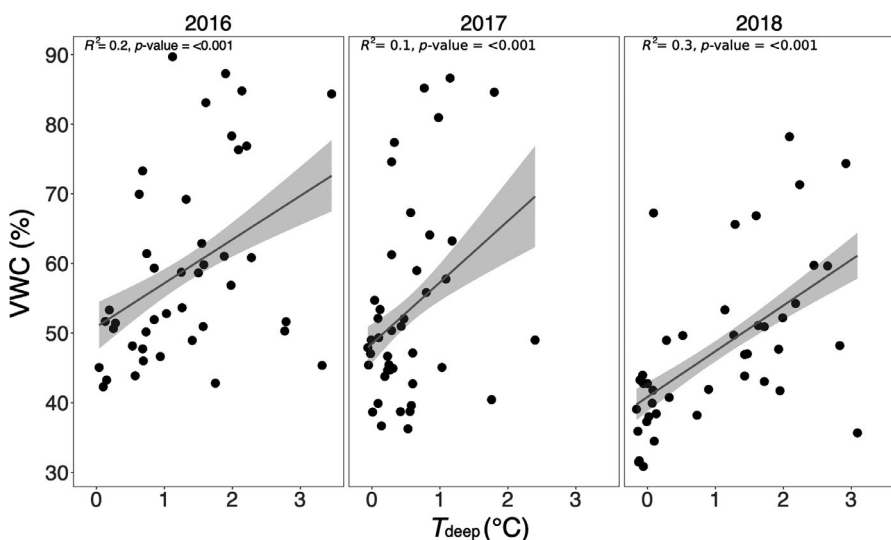
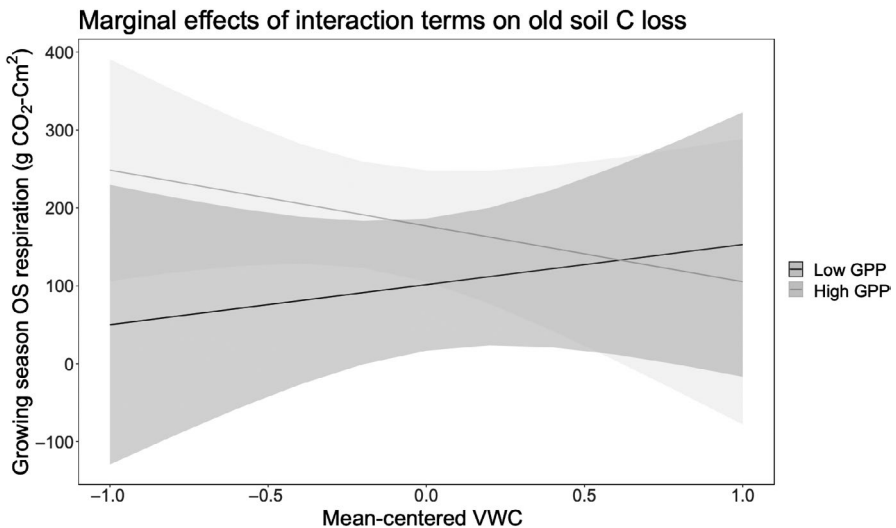


FIGURE 6 Plot-level soil volumetric water content (VWC, %) and deep soil temperature (T_{deep} , °C) measured in 2016, 2017, and 2018. The solid line shows the fit of a linear model and the shaded band represents the 95% confidence interval on the fitted values

FIGURE 7 Marginal effects of the interaction terms: GPP and VWC on growing season OS loss ($\text{g CO}_2\text{-C m}^{-2}$) in 2018. The variable VWC is mean-centered and for the continuous variable, GPP, the minimum and maximum values are chosen as the grouping levels (i.e., high and low GPP)



release of old soil C that dominated R_{eco} in 2018 occurred when soil moisture was lowest, relative to other sampling years. Our study supplements a growing body of literature showing that thermokarst formation may act to moderate microbial decomposition of old soil C when soil is highly saturated (Estop-Aragones et al., 2018; Natali et al., 2015). Nonetheless, we also found that when soil moisture decreases, a higher proportion of old soil C is vulnerable to decomposition and can become a large flux to the atmosphere.

Our analysis showed that warmer deep soils had a positive effect on $R_{\text{eco}} \Delta^{14}\text{C}$ and a negative effect the magnitude of old soil C loss, contrasting our original hypothesis that the proportion of R_{eco} from old soil C would increase with warmer deep soil temperatures. The negative relationship between deep soil temperature and old soil C loss and the positive relationship between soil VMC and deep soil temperature indicate that soil moisture and temperature are linked. Changing soil moisture can affect the propagation of heat through the soil profile (Abu-Hamdeh, 2003; Lakshmi et al., 2003), and soil temperatures in thermokarst depressions can be 2–4°C higher relative to ambient tundra soil temperatures (Osterkamp et al., 2009). Water accumulation in collapse-scar bogs and fens that occurs from ground subsidence and thermokarst features has been shown to increase soil temperature in the top 3 m of the soil profile (Jorgenson et al., 2001; O'Donnell et al., 2012). Consequently, when soil becomes drier, heat capacity and thermal conductivity decrease in highly organic soil, thus keeping deeper soil layers colder (Abu-Hamdeh & Reeder, 2000).

Thermokarst formations shape permafrost landscapes, and are increasing in frequency and magnitude due to rising air and soil temperatures (Jorgenson et al., 2001; Kokelj & Jorgenson, 2013; Lantz & Kokelj, 2008). Thermokarst features impact permafrost loss, and thus affect C dynamics in tundra ecosystems (Kokelj & Jorgenson, 2013). When ground collapses because of ice melt, local soil hydrology is affected, and subsided areas can become saturated depending on the stage of thermokarst expansion and its positioning in the landscape (O'Donnell et al., 2012). Soil moisture is one of the primary drivers of permafrost C exchange (Oberbauer et al., 2007; Oechel et al., 1998), and waterlogged conditions have been shown

to inhibit microbial soil decomposition and old soil C respiration, even in deeply thawed plots with warmer soil temperatures (Estop-Aragones et al., 2018; Natali et al., 2015). In wet sedge and moist acidic tundra, a decrease in soil moisture can increase flux rates at the ecosystem scale (Kwon et al., 2016; Oechel et al., 1998), and this trend has also been reported at Eight Mile Lake (Kwon et al., 2019; Mauritz et al., 2017; Natali et al., 2015). Water pooling in deep soil or at the permafrost table restricts microbial respiration by decreasing O_2 availability, osmoregulation, and enzyme activity (Lee et al., 2010; Lupascu, Welker, Seibt, Xu, et al., 2014; Moyano et al., 2013; Stonestrom & Rubin, 1989). As a result, microbes exhibit moisture sensitivity, and activity is optimal up to a certain threshold, after which decomposition rates decline (Moyano et al., 2013).

This soil moisture threshold can be inferred in our site based on previous partitioning studies that investigated drivers of old soil C loss. From 2009 to 2011, warmer soil temperatures decreased $R_{\text{eco}} \Delta^{14}\text{C}$ and increased the R_{eco} proportion of old soil C (Pries et al., 2016). During this period, soil warming and permafrost thaw had occurred, but there were no signs of thermokarst formation or water pooling at our site. In fact, site-level soil VWC in 2009–2011 ranged from 38.3% to 62.2%, and soil moisture was not a significant predictor of old soil C loss (Pries et al., 2016). From 2012 to 2013, soil warming continued to be a significant predictor of old soil C loss, but when warming was combined with a soil drying experiment (Natali et al., 2015), the proportion of old soil C respiration was suppressed, even though R_{eco} rates increased overall (Kwon et al., 2019). During this period, the average soil VWC ranged from 39.4 to 54.1%, indicating soils were not yet highly saturated and a decrease in moisture essentially hindered microbial decomposition at depth.

After a decade of experimental soil warming, permafrost degradation induced significant soil subsidence ranging from 1.20 to 6.12 cm yr^{-1} , causing the soil to collapse and the average water table depth to be 74% closer to the soil surface in 2018 relative to 2009 (Rodenhizer et al., 2020). By 2016, plot-level soil VWC reached a maximum of 90%, and ~25% of the plots measured from 2016 to 2018 had soil VWC greater than 60%. Our study supplements a

long-term record of old soil C loss dynamics at this site, and provides new insight on the role of soil moisture on old soil C loss. Though highly saturated soil conditions inhibit the respiration of old soil C after permafrost thaw, in a dry year, the shift in the proportional contribution of old soil C to R_{eco} represents a 30-fold increase compared to the average proportional contribution of old soil C to R_{eco} in wet years.

The variability in soil moisture created by thermokarst features in 2018 also interacted with GPP to affect old soil C loss. Though GPP had a marginal positive effect on $R_{\text{eco}} \Delta^{14}\text{C}$ (Figure S3), it was only significant when it interacted with depth of permafrost thaw and soil moisture. Previous studies determined that progressive permafrost thaw increases old soil C loss in tundra ecosystems (Pries et al., 2013; Schuur et al., 2009). However, we found that plots with a shallower active layer (~60 cm) had higher old soil C loss relative to more deeply thawed plots, despite having a smaller volume of unfrozen soil available for decomposition. While permafrost thaw affects C cycling (Schuur et al., 2008), the extent of TD is not necessarily the main driver old soil C loss (Pries et al., 2016). Permafrost degradation causes landscape feedbacks that change environmental conditions that can favor both higher GPP and enhanced microbial decomposition, which can have implications for net C exchange in permafrost. We found that plots with high GPP that were drier in 2018 had lower $R_{\text{eco}} \Delta^{14}\text{C}$, and thus greater old soil C loss during the growing season. Though higher plant productivity is projected to offset permafrost C losses through 2100 (McGuire et al., 2018), the soil C pool at our site is ~40.2 kg m⁻² (using a fixed depth of 55 cm; ref. Plaza et al., 2019) and is several orders of magnitude larger than the plant C pool (0.41–0.70 kg C m⁻²; ref. Natali et al., 2012; Salmon et al., 2016). Consequently, environmental conditions that favor higher R_{eco} in tundra may further exacerbate the effects of climate change because it is unlikely that increases in GPP will offset potential soil C losses in the long term (Plaza et al., 2019; Schädel, Koven, et al., 2018).

Comparing multiple source responses to climate feedbacks is necessary to estimate long-term C dynamics because plant and microbes respond differently to biotic and abiotic changes (Bond-Lamberty et al., 2004). We made an improvement to the commonly used dual-C isotope mixing model method that relies solely on the $\delta^{13}\text{C}$ and $\Delta^{14}\text{C}$ source end-members to partition R_{eco} , by incorporating a model-based approach that explicitly included GPP and environmental covariates to constrain source contributions. With this method, we found that the variation in $R_{\text{eco}} \Delta^{14}\text{C}$ and end-member $\Delta^{14}\text{C}$ informed the mixing model to a greater extent than the $\delta^{13}\text{C}$ data. We believe that this occurred because (1) though there was very little variation in measured $R_{\text{eco}} \Delta^{14}\text{C}$ in 2016 and 2017, the large variation in $R_{\text{eco}} \Delta^{14}\text{C}$ in 2018 was more informative than $R_{\text{eco}} \delta^{13}\text{C}$ for partitioning ecosystem respiration based on the model fit (Figure S1 and S2); (2) while the 95% CI for the old soil $\Delta^{14}\text{C}$ end-member was wide (as compared to $\Delta^{14}\text{C}$ of the other sources; Figure 2), it did not overlap with the $\Delta^{14}\text{C}$ posterior means of other sources, unlike the $\delta^{13}\text{C}$ end-member isotope data; and (3) GPP and environmental covariates may have supplied the mixing model with

more mechanistic information than the $\delta^{13}\text{C}$ data. Nonetheless, including the $\delta^{13}\text{C}$ data ensured that the predicted $\delta^{13}\text{C}$ values were constrained within the realistic range of the end-member data, and that predicted $\delta^{13}\text{C}$ values were not unreasonably biased toward certain end-members.

5 | CONCLUSION

In the initial stages of permafrost thaw, there is a positive relationship between soil temperature and old soil C loss at the ecosystem scale (Czimczik & Welker, 2010; Dorrepaal et al., 2009; Nowinski et al., 2010; Pries et al., 2013, 2016; Schuur et al., 2009). Over the long term, experimental permafrost warming introduces a soil hydrology component that, along with temperature, affect old soil C loss. After almost a decade of permafrost degradation, plots with warmer deep soil temperatures suppressed old soil C loss because they were wetter. Nonetheless, when soil moisture decreased, deep soil C became vulnerable to greater microbial decomposition and the proportion of R_{eco} from old soil C increased by 30-fold compared to the wet-year average. Our hierarchical Bayesian modeling approach to partitioning R_{eco} allowed the mixing model to be directly informed by measured GPP and environmental drivers, which helped constrain the proportional source contributions to R_{eco} . This method provided the mixing model with process-based, mechanistic information of the ecosystem that was constrained by field measurements, rather than solely relying on end-members to inform the model (Ogle et al., 2014). As permafrost systems continue to change with warmer air temperatures, we must understand the thresholds that may propel this system from a C sink to a C source to the atmosphere, as old soil C fluxes can represent a substantial amount (39%) of the growing season C flux.

ACKNOWLEDGEMENTS

We would like to thank Justin Ledman, Meghan Taylor, and Garrett Frandson for their immeasurable assistance in the field work component of this study. Furthermore, we would like to thank Christina Schädel, Brian Izbicki, Samantha Miller, Bruce Hungate, and Paul Dijkstra for their valuable suggestions and inputs on the manuscript. This work was supported by funding from the U.S. Department of Energy, Office of Biological and Environmental Research, Terrestrial Ecosystem Science (TES) Program, award DE-SC0006982 updated with DE-SC0014085 (2015–2018); National Science Foundation CAREER program, award 0747195; National Parks Inventory and Monitoring Program; National Science Foundation Bonanza Creek LTER program, award 1026415; and the Grant-In-Aid of Research from Sigma Xi, The Scientific Research Society.

DATA AVAILABILITY STATEMENT

The data that support the findings of this study are available in the supplementary materials and upon request from the corresponding author.

ORCID

- Elaine F. Pegoraro  <https://orcid.org/0000-0002-6865-8613>
- Marguerite E. Mauritz  <https://orcid.org/0000-0001-8733-9119>
- Kiona Ogle  <https://orcid.org/0000-0002-0652-8397>
- Christopher H. Ebert  <https://orcid.org/0000-0001-9450-1196>
- Edward A. G. Schuur  <https://orcid.org/0000-0002-1096-2436>

REFERENCES

- Abbott, B. W., Jones, J. B., Schuur, E. A. G., Chapin III, F. S., Bowden, W. B., Bret-Harte, M. S., Epstein, H. E., Flannigan, M. D., Harms, T. K., Hollingsworth, T. N., Mack, M. C., McGuire, A. D., Natali, S. M., Rocha, A. V., Tank, S. E., Turetsky, M. R., Vonk, J. E., Wickland, K. P., Aiken, G. R., ... Zimov, S. (2016). Biomass offsets little or none of permafrost carbon release from soils, streams, and wildfire: An expert assessment. *Environmental Research Letters*, 11(3), 034014. <https://doi.org/10.1088/1748-9326/11/3/034014>
- Abu-Hamdeh, N. H. (2003). Thermal properties of soils as affected by density and water content. *Biosystems Engineering*, 86, 97–102. [https://doi.org/10.1016/S1537-5110\(03\)00112-0](https://doi.org/10.1016/S1537-5110(03)00112-0)
- Abu-Hamdeh, N. H., & Reeder, R. C. (2000). Soil thermal conductivity: Effects of density, moisture, salt concentration, and organic matter. *Soil Science Society of America Journal*, 64, 1285–1290. <https://doi.org/10.2136/sssaj2000.6441285x>
- Allen, M. R., Dube, O. P., Solecki, W., Aragón-Durand, F., Cramer, W., Humphreys, S., Kainuma, M., Kala, J., Mahowald, N., Mulugetta, Y., Perez, R., Wairiu, M., & Zickfeld, K. (2019). Framing and context. In V. Masson-Delmotte, P. Zhai, H.-O. Portner, D. Roberts, J. Skea, P. R. Shukla, A. Pirani, W. Moufouma-Okia, C. Péan, R. Pidcock, S. Connors, J. B. R. Matthews, Y. Chen, X. Zhou, M. I. Gomis, E. Lonnoy, T. Maycock, M. Tignor, & T. Waterfield (Eds.), *Global warming of 1.5°C. An IPCC special report on the impacts of global warming of 1.5°C above pre-industrial levels and related global greenhouse gas emission pathways, in the context of strengthening the global response to the threat of climate change, sustainable development, and efforts to eradicate poverty* (Vol. 84). Intergovernmental Panel on Climate Change (IPCC).
- Bates, D., Machler, M., Bolker, B. M., & Walker, S. C. (2015). Fitting linear mixed-effects models using lme4. *Journal of Statistical Software*, 67, 1–48. <https://doi.org/10.18637/jss.v067.i01>
- Bauer, J. E., Williams, P. M., & Druffel, E. R. M. (1992). Recovery of sub-milligram quantities of carbon-dioxide from gas streams by molecular-sieve for subsequent determination of isotopic (C-13 and C-14) natural abundances. *Analytical Chemistry*, 64, 824–827. <https://doi.org/10.1021/ac00031a024>
- Bond-Lamberty, B., Wang, C. K., & Gower, S. T. (2004). A global relationship between the heterotrophic and autotrophic components of soil respiration? *Global Change Biology*, 10, 1756–1766. <https://doi.org/10.1111/j.1365-2486.2004.00816.x>
- Bowling, D. R., Pataki, D. E., & Randerson, J. T. (2008). Carbon isotopes in terrestrial ecosystem pools and CO₂ fluxes. *New Phytologist*, 178, 24–40. <https://doi.org/10.1111/j.1469-8137.2007.02342.x>
- Bracho, R., Natali, S., Pegoraro, E., Crummer, K. G., Schädel, C., Celis, G., Hale, L., Wu, L. Y., Yin, H. Q., Tiedje, J. M., Konstantinidis, K. T., Luo, Y. Q., Zhou, J. Z., & Schuur, E. A. G. (2016). Temperature sensitivity of organic matter decomposition of permafrost-region soils during laboratory incubations. *Soil Biology and Biochemistry*, 97, 1–14. <https://doi.org/10.1016/j.soilbio.2016.02.008>
- Chapin, F. S., Woodwell, G. M., Randerson, J. T., Rastetter, E. B., Lovett, G. M., Baldocchi, D. D., Clark, D. A., Harmon, M. E., Schimel, D. S., Valentini, R., Wirth, C., Aber, J. D., Cole, J. J., Goulden, M. L., Harden, J. W., Heimann, M., Howarth, R. W., Matson, P. A., McGuire, A. D., ... Schulze, E. D. (2006). Reconciling carbon-cycle concepts, terminology, and methods. *Ecosystems*, 9, 1041–1050. <https://doi.org/10.1007/s10021-005-0105-7>
- Czimczik, C. I., & Welker, J. M. (2010). Radiocarbon content of CO₂ respired from high Arctic tundra in Northwest Greenland. *Arctic Antarctic and Alpine Research*, 42, 342–350.
- Davidson, E. A., & Janssens, I. A. (2006). Temperature sensitivity of soil carbon decomposition and feedbacks to climate change. *Nature*, 440, 165–173. <https://doi.org/10.1038/nature04514>
- Deane-Coe, K. K., Mauritz, M., Celis, G., Salmon, V. G., Crummer, K. G., Natali, S. M., & Schuur, E. A. G. (2015). Experimental warming alters productivity and isotopic signatures of tundra mosses. *Ecosystems*, 18, 1070–1082. <https://doi.org/10.1007/s10021-015-9884-7>
- Dorrepael, E., Toet, S., van Logtestijn, R. S. P., Swart, E., van de Weg, M. J., Callaghan, T. V., & Aerts, R. (2009). Carbon respiration from subsurface peat accelerated by climate warming in the subarctic. *Nature*, 460, 616–619. <https://doi.org/10.1038/nature08216>
- Dudziak, A., & Halas, S. (1996). Diurnal cycle of carbon isotope ratio in soil CO₂ in various ecosystems. *Plant and Soil*, 183, 291–299. <https://doi.org/10.1007/bf00011444>
- Estop-Aragones, C., Czimczik, C. I., Heffernan, L., Gibson, C., Walker, J. C., Xu, X. M., & Olefeldt, D. (2018). Respiration of aged soil carbon during fall in permafrost peatlands enhanced by active layer deepening following wildfire but limited following thermokarst. *Environmental Research Letters*, 13, 085002. <https://doi.org/10.1088/1748-9326/aad5f0>
- Fry, B. (2007). Using stable isotope tracers. In *Stable isotope ecology* (1st ed, pp. 40–75). Springer. https://doi.org/10.1007/0-387-33745-8_3
- Gelman, A., Carlin, J. B., Stern, H. S., & Rubin, D. B. (2004). *Bayesian data analysis*. Chapman and Hall/CRC Press.
- Gelman, A., Carlin, J., Stern, H., & Rubin, D. (2014). *Bayesian data analysis* (3rd ed.). Chapman and Hall.
- Gelman, A., & Rubin, D. B. (1992). Inference from iterative simulation using multiple sequences. *Statistical Science*, 7, 457–472. <https://doi.org/10.1214/ss/1177011136>
- Hardie, S. M. L., Garnett, M. H., Fallick, A. E., Rowland, A. P., & Ostle, N. J. (2005). Carbon dioxide capture using a zeolite molecular sieve sampling system for isotopic studies (C-13 and C-14) of respiration. *Radiocarbon*, 47, 441–451. <https://doi.org/10.1017/s003382220035220>
- Hobbie, S. E., & Chapin, F. S. (1998). Response of tundra plant biomass, aboveground production, nitrogen, and CO₂ flux to experimental warming. *Ecology*, 79, 1526–1544. <https://doi.org/10.2307/176774>
- Hugelius, G., Strauss, J., Zubrzycki, S., Harden, J. W., Schuur, E. A. G., Ping, C.-L., Schirrmeister, L., Grosse, G., Michaelson, G. J., Koven, C. D., O'Donnell, J. A., Elberling, B., Mishra, U., Camill, P., Yu, Z., Palmtag, J., & Kuhry, P. (2014). Estimated stocks of circumpolar permafrost carbon with quantified uncertainty ranges and identified data gaps. *Biogeosciences*, 11, 6573–6593. <https://doi.org/10.5194/bg-11-6573-2014>
- Jorgenson, M. T., Racine, C. H., Walters, J. C., & Osterkamp, T. E. (2001). Permafrost degradation and ecological changes associated with a warming climate in central Alaska. *Climatic Change*, 48, 551–579. <https://doi.org/10.1023/a:1005667424292>
- Keeling, C. D. (1958). The concentration and isotopic abundances of atmospheric carbon dioxide in rural areas. *Geochimica et Cosmochimica Acta*, 13, 322–334. [https://doi.org/10.1016/0016-7037\(58\)90033-4](https://doi.org/10.1016/0016-7037(58)90033-4)
- Keeling, C. D. (1961). The concentration and isotopic abundances of carbon dioxide in rural and marine air. *Geochimica et Cosmochimica Acta*, 24, 277–298. [https://doi.org/10.1016/0016-7037\(61\)90023-0](https://doi.org/10.1016/0016-7037(61)90023-0)
- Kokelj, S. V., & Jorgenson, M. T. (2013). Advances in thermokarst research. *Permafrost and Periglacial Processes*, 24, 108–119. <https://doi.org/10.1002/ppp.1779>

- Kwon, M. J., Heimann, M., Kolle, O., Luus, K. A., Schuur, E. A. G., Zimov, N., Zimov, S. A., & Gockede, M. (2016). Long-term drainage reduces CO₂ uptake and increases CO₂ emission on a Siberian floodplain due to shifts in vegetation community and soil thermal characteristics. *Biogeosciences*, 13, 4219–4235. <https://doi.org/10.5194/bg-13-4219-2016>
- Kwon, M. J., Natali, S. M., Pries, C. E. H., Schuur, E. A. G., Steinhof, A., Crummer, K. G., Zimov, N., Zimov, S. A., Heimann, M., Kolle, O., & Gockede, M. (2019). Drainage enhances modern soil carbon contribution but reduces old soil carbon contribution to ecosystem respiration in tundra ecosystems. *Global Change Biology*, 25, 1315–1325. <https://doi.org/10.1111/gcb.14578>
- Lakshmi, V., Jackson, T. J., & Zehrfuhs, D. (2003). Soil moisture-temperature relationships: Results from two field experiments. *Hydrological Processes*, 17, 3041–3057. <https://doi.org/10.1002/hyp.1275>
- Lantz, T. C., & Kokelj, S. V. (2008). Increasing rates of retrogressive thaw slump activity in the Mackenzie Delta region, NWT, Canada. *Geophysical Research Letters*, 35. <https://doi.org/10.1029/2007gl032433>
- Lawrence, D. M., Koven, C. D., Swenson, S. C., Riley, W. J., & Slater, A. G. (2015). Permafrost thaw and resulting soil moisture changes regulate projected high-latitude CO₂ and CH₄ emissions. *Environmental Research Letters*, 10, 094011. <https://doi.org/10.1088/1748-9326/10/9/094011>
- Lee, H., Schuur, E. A. G., & Vogel, J. G. (2010). Soil CO₂ production in upland tundra where permafrost is thawing. *Journal of Geophysical Research: Biogeosciences*, 115. <https://doi.org/10.1029/2008jg000906>
- Li, B. X., Heijmans, M. M. P. D., Blok, D., Wang, P., Karsanaev, S. V., Maximov, T. C., van Huissteden, J., & Berendse, F. (2017). Thaw pond development and initial vegetation succession in experimental plots at a Siberian lowland tundra site. *Plant and Soil*, 420, 147–162. <https://doi.org/10.1007/s11104-017-3369-8>
- Lin, G. H., & Ehleringer, J. R. (1997). Carbon isotopic fractionation does not occur during dark respiration in C-3 and C-4. *Plant Physiology*, 114, 391–394. <https://doi.org/10.1104/pp.114.1.391>
- Lüdecke, D. (2018). sjmisc: Data and variable transformation functions. *Journal of Open Source Software*, 3, 754. <https://doi.org/10.21105/joss.00754>
- Lunn, D., Spiegelhalter, D., Thomas, A., & Best, N. (2009). The BUGS project: Evolution, critique and future directions (with discussion). *Statistics in Medicine*, 28, 3049–3082.
- Lupascu, M., Welker, J. M., Seibt, U., Maseyk, K., Xu, X., & Czimczik, C. I. (2014). High Arctic wetting reduces permafrost carbon feedbacks to climate warming. *Nature Climate Change*, 4, 51–55. <https://doi.org/10.1038/nclimate2058>
- Lupascu, M., Welker, J. M., Seibt, U., Xu, X., Velicogna, I., Lindsey, D. S., & Czimczik, C. I. (2014). The amount and timing of precipitation control the magnitude, seasonality and sources (C-14) of ecosystem respiration in a polar semi-desert, northwestern Greenland. *Biogeosciences*, 11, 4289–4304. <https://doi.org/10.5194/bg-11-4289-2014>
- Mauritz, M., Bracho, R., Celis, G., Hutchings, J., Natali, S. M., Pegoraro, E., Salmon, V. G., Schädel, C., Webb, E. E., & Schuur, E. A. G. (2017). Non-linear CO₂ flux response to seven years of experimentally induced permafrost thaw. *Global Change Biology*, 23, 3646–3666. <https://doi.org/10.1111/gcb.13661>
- Mauritz, M., Celis, G., Ebert, C., Hutchings, J., Ledman, J., Natali, S. M., Pegoraro, E., Salmon, V. G., Schädel, C., Taylor, M., & Schuur, E. A. G. (2019). Using stable carbon isotopes of seasonal ecosystem respiration to determine permafrost carbon loss. *Journal of Geophysical Research: Biogeosciences*, 124, 46–60. <https://doi.org/10.1029/2018JG004619>
- McGuire, A. D., Lawrence, D. M., Koven, C., Clein, J. S., Burke, E., Chen, G. S., Jafarov, E., MacDougall, A. H., Marchenko, S., Nicolsky, D., Peng, S. S., Rinke, A., Cais, P., Gouttevin, I., Hayes, D. J., Ji, D. Y., Krinner, G., Moore, J. C., Romanovsky, V., ... Zhuang, Q. L. (2018). Dependence of the evolution of carbon dynamics in the northern permafrost region on the trajectory of climate change. *Proceedings of the National Academy of Sciences of the United States of America*, 115, 3882–3887. <https://doi.org/10.1073/pnas.1719903115>
- Moyano, F. E., Manzoni, S., & Chenu, C. (2013). Responses of soil heterotrophic respiration to moisture availability: An exploration of processes and models. *Soil Biology and Biochemistry*, 59, 72–85. <https://doi.org/10.1016/j.soilbio.2013.01.002>
- Natali, S. M., Schuur, E. A. G., Mauritz, M., Schade, J. D., Celis, G., Crummer, K. G., Johnston, C., Krapek, J., Pegoraro, E., Salmon, V. G., & Webb, E. E. (2015). Permafrost thaw and soil moisture driving CO₂ and CH₄ release from upland tundra. *Journal of Geophysical Research: Biogeosciences*, 120, 525–537. <https://doi.org/10.1002/2014jg002872>
- Natali, S. M., Schuur, E. A. G., & Rubin, R. L. (2012). Increased plant productivity in Alaskan tundra as a result of experimental warming of soil and permafrost. *Journal of Ecology*, 100, 488–498. <https://doi.org/10.1111/j.1365-2745.2011.01925.x>
- Natali, S. M., Schuur, E. A. G., Trucco, C., Pries, C. E. H., Crummer, K. G., & Lopez, A. F. B. (2011). Effects of experimental warming of air, soil and permafrost on carbon balance in Alaskan tundra. *Global Change Biology*, 17, 1394–1407. <https://doi.org/10.1111/j.1365-2486.2010.02303.x>
- Nauta, A. L., Heijmans, M. M. P. D., Blok, D., Limpens, J., Elberling, B., Gallagher, A., Li, B. X., Petrov, R. E., Maximov, T. C., van Huissteden, J., & Berendse, F. (2015). Permafrost collapse after shrub removal shifts tundra ecosystem to a methane source. *Nature Climate Change*, 5, 67–70. <https://doi.org/10.1038/nclimate2446>
- Nowinski, N. S., Taneva, L., Trumbore, S. E., & Welker, J. M. (2010). Decomposition of old organic matter as a result of deeper active layers in a snow depth manipulation experiment. *Oecologia*, 163, 785–792. <https://doi.org/10.1007/s00442-009-1556-x>
- Oberbauer, S. F., Tweedie, C. E., Welker, J. M., Fahnestock, J. T., Henry, G. H. R., Webber, P. J., Hollister, R. D., Walker, M. D., Kuchy, A., Elmore, E., & Starr, G. (2007). Tundra CO₂ fluxes in response to experimental warming across latitudinal and moisture gradients. *Ecological Monographs*, 77, 221–238. <https://doi.org/10.1890/06-0649>
- O'Donnell, J. A., Jorgenson, M. T., Harden, J. W., McGuire, A. D., Kanevskiy, M. Z., & Wickland, K. P. (2012). The effects of permafrost thaw on soil hydrologic, thermal, and carbon dynamics in an Alaskan peatland. *Ecosystems*, 15, 213–229. <https://doi.org/10.1007/s10021-011-9504-0>
- Oechel, W. C., Vourlitis, G. L., Hastings, S. J., Ault, R. P., & Bryant, P. (1998). The effects of water table manipulation and elevated temperature on the net CO₂ flux of wet sedge tundra ecosystems. *Global Change Biology*, 4, 77–90. <https://doi.org/10.1046/j.1365-2486.1998.00110.x>
- Ogle, K., Barber, J. J., & Sartor, K. (2013). Feedback and modularization in a Bayesian meta-analysis of tree traits affecting forest dynamics. *Bayesian Analysis*, 8, 133–168. <https://doi.org/10.1214/13-BA806>
- Ogle, K., & Pendall, E. (2015). Isotope partitioning of soil respiration: A Bayesian solution to accommodate multiple sources of variability. *Journal of Geophysical Research: Biogeosciences*, 120, 221–236. <https://doi.org/10.1002/2014JG002794>
- Ogle, K., Tucker, C., & Cable, J. M. (2014). Beyond simple linear mixing models: Process-based isotope partitioning of ecological processes. *Ecological Applications*, 24, 181–195. <https://doi.org/10.1890/12-1970.1>
- Osterkamp, T. E., Jorgenson, M. T., Schuur, E. A. G., Shur, Y. L., Kanevskiy, M. Z., Vogel, J. G., & Tumskoy, V. E. (2009). Physical and ecological changes associated with warming permafrost and thermokarst in interior Alaska. *Permafrost and Periglacial Processes*, 20, 235–256. <https://doi.org/10.1002/ppp.656>

- Osterkamp, T. E., & Romanovsky, V. E. (1999). Evidence for warming and thawing of discontinuous permafrost in Alaska. *Permafrost and Periglacial Processes*, 10, 17–37. [https://doi.org/10.1002/\(SICI\)1099-1530\(199901/03\)10:1%3C17:AID-PPP303%3E3.0.CO;2-4](https://doi.org/10.1002/(SICI)1099-1530(199901/03)10:1%3C17:AID-PPP303%3E3.0.CO;2-4)
- Overland, J. E., Hanna, E., Hanssen-Bauer, I., Kim, S.-J., Walsh, J. E., Wang, M., Bhatt, U. S., Thoman, R. L., & Ballinger, T. J. (2019). Arctic Ocean primary productivity: Surface air temperature. In J. Richter-Menge, M. L. Druckenmiller, and M. Jeffries, (Eds.), *Arctic report card 2019*. Retrieved from <https://www.arctic.noaa.gov/Report-Card>
- Pinheiro, J. C., & Bates, D. M. (2000). Extending the basic linear mixed effects model. In *Mixed effects models in S and S-PLUS* (1st ed., pp. XVI–528). Springer-Verlag.
- Plaza, C., Pegoraro, E., Bracho, R., Celis, G., Crummer, K. G., Hutchings, J. A., Hicks Pries, C. E., Mauritz, M., Natali, S. M., Salmon, V. G., Schädel, C., Webb, E. E., & Schuur, E. A. G. (2019). Direct observation of permafrost degradation and rapid soil carbon loss in tundra. *Nature Geoscience*, 12, 627–631. <https://doi.org/10.1038/s41561-019-0387-6>
- Pries, C. E. H., Schuur, E. A. G., & Crummer, K. G. (2012). Holocene carbon stocks and carbon accumulation rates altered in soils undergoing permafrost thaw. *Ecosystems*, 15, 162–173. <https://doi.org/10.1007/s10021-011-9500-4>
- Pries, C. E. H., Schuur, E. A. G., & Crummer, K. G. (2013). Thawing permafrost increases old soil and autotrophic respiration in tundra: Partitioning ecosystem respiration using delta C-13 and Delta C-14. *Global Change Biology*, 19, 649–661. <https://doi.org/10.1111/gcb.12058>
- Pries, C. E. H., Schuur, E. A. G., Natali, S. M., & Crummer, K. G. (2016). Old soil carbon losses increase with ecosystem respiration in experimentally thawed tundra. *Nature Climate Change*, 6, 214–218. <https://doi.org/10.1038/nclimate2830>
- R Development Core Team. (2015). *R: A language and environment for statistical computing*. R Foundation for Statistical Computing.
- Rodenizer, H., Ledman, J., Mauritz, M., Natali, S., Pegoraro, E., Plaza, C., Romano, E., Schädel, C., Taylor, M., & Schuur, E. A. G. (2020). Carbon thaw rate doubles when accounting for subsidence in a permafrost warming experiment. *Journal of Geophysical Research: Biogeosciences*, 125, e2019JG005528. <https://doi.org/10.1029/2019jg005528>
- Romanovsky, V. E., Smith, S. L., Christiansen, H. H., Shiklomanov, N. I., Streletskiy, D. A., Drozdov, D. S., Oberman, N. G., Kholodov, A. L., & Marchenko, S. S. (2012). *Permafrost [in Arctic Report Card]*. NOAA.
- Romanovsky, V. E., Smith, S. L., Shiklomanov, N. I., Streletskiy, D. A., Isaksen, K., Kholodov, A. L., Christiansen, H. H., Drozdov, D. S., Malkova, G. V., & Marchenko, S. S. (2017). [Arctic] Terrestrial permafrost [in "State of the climate in 2016"]. *Bulletin of the American Meteorological Society (Supplement)*, 98(8), S147–S151.
- Salmon, V. G., Schädel, C., Bracho, R., Pegoraro, E., Celis, G., Mauritz, M., Mack, M. C., & Schuur, E. A. G. (2018). Adding depth to our understanding of nitrogen dynamics in permafrost soils. *Journal of Geophysical Research: Biogeosciences*, 123, 2497–2512. <https://doi.org/10.1029/2018jg004518>
- Salmon, V. G., Soucy, P., Mauritz, M., Celis, G., Natali, S. M., Mack, M. C., & Schuur, E. A. G. (2016). Nitrogen availability increases in a tundra ecosystem during five years of experimental permafrost thaw. *Global Change Biology*, 22, 1927–1941. <https://doi.org/10.1111/gcb.13204>
- Schädel, C., Koven, C. D., Lawrence, D. M., Celis, G., Garnello, A. J., Hutchings, J., Mauritz, M., Natali, S. M., Pegoraro, E., Rodenizer, H., Salmon, V. G., Taylor, M. A., Webb, E. E., Wieder, W. R., & Schuur, E. A. G. (2018). Divergent patterns of experimental and model-derived permafrost ecosystem carbon dynamics in response to Arctic warming. *Environmental Research Letters*, 13. <https://doi.org/10.1088/1748-9326/aae0ff>
- Schuur, E. A. G., Bockheim, J., Canadell, J. G., Euskirchen, E., Field, C. B., Goryachkin, S. V., Hagemann, S., Kuhry, P., Lafleur, P. M., Lee, H., Mazhitova, G., Nelson, F. E., Rinke, A., Romanovsky, V. E., Shiklomanov, N., Tarnocai, C., Venevsky, S., Vogel, J. G., & Zimov, S. A. (2008). Vulnerability of permafrost carbon to climate change: Implications for the global carbon cycle. *BioScience*, 58, 701–714. <https://doi.org/10.1641/B580807>
- Schuur, E. A. G., Carbone, M. S., Hicks Pries, C. E., Hopkins, F. M., & Natali, S. M. (2016). In E. A. G. Schuur, E. R. M. Druffel & S. E. Trumbore (Eds.), *Radiocarbon in terrestrial systems*. In *Radiocarbon and climate change* (pp. 167–220). Springer.
- Schuur, E. A. G., Crummer, K. G., Vogel, J. G., & Mack, M. C. (2007). Plant species composition and productivity following permafrost thaw and thermokarst in Alaskan tundra. *Ecosystems*, 10, 280–292. <https://doi.org/10.1007/s10021-007-9024-0>
- Schuur, E. A. G., & Mack, M. C. (2018). Ecological response to permafrost thaw and consequences for local and global ecosystem services. *Annual Review of Ecology, Evolution, and Systematics*, 49(49), 279–301. <https://doi.org/10.1146/annurev-ecolsys-121415-032349>
- Schuur, E. A. G., McGuire, A. D., Romanovsky, V. E., Schädel, C., & Mack, M. C. (2018). Chapter 11: Arctic and boreal carbon. U.S. Global Change Research Program.
- Schuur, E. A. G., McGuire, A. D., Schädel, C., Grosse, G., Harden, J. W., Hayes, D. J., Hugelius, G., Koven, C. D., Kuhry, P., Lawrence, D. M., Natali, S. M., Olefeldt, D., Romanovsky, V. E., Schaefer, K., Turetsky, M. R., Treat, C. C., & Vonk, J. E. (2015). Climate change and the permafrost carbon feedback. *Nature*, 520, 171–179. <https://doi.org/10.1038/nature14338>
- Schuur, E. A. G., & Trumbore, S. E. (2006). Partitioning sources of soil respiration in boreal black spruce forest using radiocarbon. *Global Change Biology*, 12, 165–176. <https://doi.org/10.1111/j.1365-2486.2005.01066.x>
- Schuur, E. A. G., Trumbore, S. E., Mack, M. C., & Harden, J. W. (2003). Isotopic composition of carbon dioxide from a boreal forest fire: Inferring carbon loss from measurements and modeling. *Global Biogeochemical Cycles*, 17. <https://doi.org/10.1029/2001GB001840>
- Schuur, E. A. G., Vogel, J. G., Crummer, K. G., Lee, H., Sickman, J. O., & Osterkamp, T. E. (2009). The effect of permafrost thaw on old carbon release and net carbon exchange from tundra. *Nature*, 459, 556–559. <https://doi.org/10.1038/nature08031>
- Shaver, G. R., Chapin, F., & Gartner, B. L. (1986). Factors limiting seasonal growth and peak biomass accumulation in *Eriophorum-Vaginatum* in Alaskan Tussock Tundra. *Journal of Ecology*, 74, 257–278. <https://doi.org/10.2307/2260362>
- Spiegelhalter, D. J., Best, N. G., Carlin, B. R., & van der Linde, A. (2002). Bayesian measures of model complexity and fit. *Journal of the Royal Statistical Society Series B: Statistical Methodology*, 64, 583–616. <https://doi.org/10.1111/1467-9868.00353>
- Stonestrom, D. A., & Rubin, J. (1989). Air permeability and trapped-air content in 2 soils. *Water Resources Research*, 25, 1959–1969. <https://doi.org/10.1029/wr025i009p01959>
- Stuiver, M., & Polach, H. A. (1977). Discussion: Reporting of 14C data. *Radiocarbon*, 19, 355–363. <https://doi.org/10.1017/s003382200003672>
- Sturtz, S., Ligges, U., & Gelman, A. (2005). R2WinBUGS: A package for running WinBUGS from R. *Journal of Statistical Software*, 12, 1–16. <https://doi.org/10.18637/jss.v012.i03>
- Tarnocai, C., Canadell, J. G., Schuur, E., Kuhry, P., Mazhitova, G., & Zimov, S. (2009). Soil organic carbon pools in the northern circumpolar permafrost region. *Global Biogeochemical Cycles*, 23. <https://doi.org/10.1029/2008gb003327>
- Taylor, M., Schuur, E. A. G., Mauritz, M., Pegoraro, E., Salmon, V. G., & Natali, S. M. (2018). Eight Mile Lake Research Watershed, Carbon in Permafrost Experimental Heating and Drying Research (DryPEHR): Peak growing season aboveground biomass 2011–2017. University of Alaska Fairbanks Bonanza Creek LTER.
- Trumbore, S. (2000). Age of soil organic matter and soil respiration: Radiocarbon constraints on belowground C dynamics. *Ecological*

- Applications, 10, 399–411. [https://doi.org/10.1890/1051-0761\(2000\)010%5B0399:aosoma%5D2.0.co;2](https://doi.org/10.1890/1051-0761(2000)010%5B0399:aosoma%5D2.0.co;2)
- Trumbore, S. (2006). Carbon respired by terrestrial ecosystems – Recent progress and challenges. *Global Change Biology*, 12, 141–153. <https://doi.org/10.1111/j.1365-2486.2006.01067.x>
- Trumbore, S. E., Sierra, C. A., & Hicks Pries, C. E. (2016). Radiocarbon nomenclature, theory, models, and interpretation: Measuring age, determining cycling rates, and tracing source pools. In E. A. G. Schuur, E. R. M. Druffel, & S. E. Trumbore (Eds.), *Radiocarbon and climate change* (pp. 45–82). Springer.
- Trumbore, S. E., Xu, X., Santos, G. M., Czimczik, C. I., Beaupre, S. R., Pack, M. A., Hopkins, F. M., Stills, A., Lupascu, M., & Ziolkowski, L. (2016). Preparation for radiocarbon analysis. In E. A. G. Schuur, E. R. M. Druffel, & S. E. Trumbore (Eds.), *Radiocarbon and climate change* (pp. 279–308). Springer.
- Vogel, J. S., Nelson, D. E., & Southon, J. R. (1987). C-14 background levels in an accelerator mass-spectrometry system. *Radio-carbon*, 29, 323–333. <https://doi.org/10.1017/s0033822200043733>
- Zimov, S. A., Schuur, E. A. G., & Chapin, F. S. (2006). Permafrost and the global carbon budget. *Science*, 312, 1612–1613.

SUPPORTING INFORMATION

Additional supporting information may be found online in the Supporting Information section.

How to cite this article: Pegoraro EF, Mauritz ME, Ogle K, Ebert CH, Schuur EA. Lower soil moisture and deep soil temperatures in thermokarst features increase old soil carbon loss after 10 years of experimental permafrost warming. *Glob Change Biol*. 2021;27:1293–1308. <https://doi.org/10.1111/gcb.15481>